

# **Radioluminescence properties of the CdSe/ZnS Quantum Dot nanocrystals with analysis of long-memory trends.**

**D. Nikolopoulos<sup>a</sup>, I. Valais<sup>b,\*</sup>, C. Michail<sup>b</sup>, A. Bakas<sup>c</sup>, C. Fountzoula<sup>d</sup>, D. Cantzos<sup>e</sup>, D. Bhattacharyya<sup>f</sup>, I. Sianoudis<sup>g</sup>, G. Fountos<sup>b</sup>, P. Yannakopoulos<sup>a</sup>, G. Panayiotakis<sup>h</sup> and I. Kandarakis<sup>b</sup>**

<sup>a</sup> *Piraeus University of Applied Sciences, Department of Electronic Computer Systems Engineering, Petrou Ralli & Thivon 250, GR-12244 Aigaleo, Greece*

<sup>b</sup> *Radiation Physics, Materials Technology and Biomedical Imaging Laboratory, Department of Biomedical Engineering, Technological Educational Institute of Athens, Egaleo, 122 10 Athens, Greece*

<sup>c</sup> *Department of Medical Radiologic Technology, Technological Educational Institute of Athens, 122 10 Athens, Greece*

<sup>d</sup> *Department of Medical Laboratories Faculty of Health and Caring Profession, Technological Educational Institute of Athens, 122 10 Athens, Greece*

<sup>e</sup> *Piraeus University of Applied Sciences (TEI of Piraeus), Department of Automation Engineering, Petrou Ralli & Thivon 250, GR-12244 Aigaleo, Greece*

<sup>f</sup> *Cranfield University, Surface Engineering and Nanotechnology Institute, Bedfordshire, MK43 0AL, United Kingdom*

<sup>g</sup> *Department of Optics and Optometry, Technological Educational Institute of Athens, 122  
10 Athens, Greece*

<sup>h</sup> *University of Patras, School of Medicine, Department of Medical Physics, GR-15310,  
Rion, Greece*

## ABSTRACT

This paper reports radioluminescence properties of the CdSe/ZnS quantum dots. Three quantum dot samples were prepared with concentrations  $14.2 \times 10^{-5}$  mg/mL,  $21.3 \times 10^{-5}$  mg/mL and  $28.5 \times 10^{-5}$  mg/mL, respectively. The ultraviolet induced emission spectra of CdSe/ZnS dots exhibited a peak at 550 nm ranging between 450 nm and 650 nm. Discrepancies observed between 250 nm and 450 nm were attributed to the solvent and cuvette. The absolute efficiency calculated from random fractional-Gaussian luminescence segments varied. Long-memory fractional-Brownian segments were also found. The quantum dot solution with concentration of  $21.3 \times 10^{-5}$  mg/mL exhibited the maximum absolute efficiency value at 90 kVp. The CdSe/ZnS dots have demonstrated potential for detection of X-rays in the medical imaging energy range.

Corresponding author.

E-mail address: [valais@teiath.gr](mailto:valais@teiath.gr) (I. Valais)

**KEYWORDS:** *Quantum Dots; Absolute Luminescence Efficiency; CdSe/ZnS*

## **1. Introduction**

Radiation based Medical Imaging (RMI) has facilitated several fields of medicine by achieving increased levels of diagnostic accuracy. However, despite the on-going progress in RMI, it remains entangled to accomplish low-cost designs of enhanced image quality and low radiation risk to human (Van Eijk, 2008). Both, the experimental and the computational techniques, offer an extensive methodology to incorporate new and innovative RMI designs, especially, in the modalities which utilise radiation sensors (Knoll, 2010). The current approaches aim to employ new fast light-emitting materials with efficient coupling to state-of-the art optical sensors (Michail, 2015a). In particular, the new methods look promising to integrate novel nanophosphors with appealing characteristics, well-established Complementary Metal Oxide Semiconductors (CMOS), e.g. Si-CMOS-based technology (Seferis et al., 2013, Michail et al., 2015b) and Quantum Dots (QDs) as gain materials (Krasnyj et al., 2007, Del Sordo et al., 2009, Hobson et al., 2011). The related research extends both at the spectral emission and the radiation detection domains (Michail et al., 2007, Michail et al., 2014a, David et al., 2016). Apart from X-ray imaging, the phosphor-based sensing materials have been employed also in optoelectronic devices, nuclear medicine, dosimetry and in high energy physics experiments (Beierholm et al., 2008, Valais et al., 2010, Kobayashi et al., 2012, Yanagida et al., 2014). It becomes evident that the radiation sensors constitute critical structural parts of detectors of RMI systems (Blasse and Grabmaier, 1994, Kandarakis and Cavouras 2001, Rodnyi, 2001, Doi, 2006, Gupta et al., 2006, Ross et al., 2006, Van Eijk, 2008, Yaffe et al.,

2008, Michail et al., 2013, 2014b, David et al., 2016). Optimisation of existing RMI materials can be achieved by introducing new materials of higher radiation efficiency and better optical properties (Blasse and Grabmaier, 1994, Seferis et al., 2014, Prochazkova et al., 2016). Simultaneously, the novel designs need to be explored through a combination of modelling and experimentation. Noteworthy advances in this field of research include the construction of sensors of small size (Rodnyi, 2001, Michail et al., 2015a), nanophosphors (Kalyvas et al., 2011, Seferis et al., 2014, 2015) and QDs (Zych et al., 2003, Kim et al., 2007, Konstantatos et al., 2007, Del Sordo et al., 2009, Rauch et al., 2009, Stodilka et al., 2009, Baharin et al., 2010, Malyukin, 2010, Hobson et al., 2011, Konstantatos and Sargent, 2011, Lawrence et al., 2012). QDs resemble particle size of the order of 1nm-20nm (Goncharova et al., 2004). Due to their unique optical and electrical properties they have been already utilised in optoelectronic sensors (Guo et al., 2000, Eychmuller, 2000, Ma et al., 2003, Wang et al., 2006, Gbur et al., 2013), as radiation sensors (Sordo et al., 2009, Stodilka et al., 2009, Baharin et al., 2010, Hobson et al., 2011, Nistor et al., 2013, Sahi and Chen 2013) and theranostics in nuclear medicine (Assadi et al., 2011). Recent studies suggest also that QDs can be employed in optical diffusion applications of high sensitivity (e.g. in nuclear medical imaging), nuclear physics to X-ray and gamma-ray astronomy (Pang et al., 2005, Voitenko et al., 2007, Del Sordo et al., 2009, Klassen et al., 2009, Xing et al., 2009), as well as in modalities where high light spatial resolution is required (e.g. in X-ray projection medical imaging) (Kandarakis et al., 2005, Jacobsohn et al., 2007, Del Sordo et al., 2009, Stodilka et al., 2009, Baharin et al., 2010, Hobson et al., 2011, Seferis et al., 2014, 2015).

QDs can be grouped also as semiconductor sensors that have progressed during the last decade. Moreover, QD-polymer composite films scintillate upon exposure to ionising radiation (Dai et al., 2002, Letant and Wang, 2006a, 2006b), and this has been attributed to the transportation of charge within the QD polymer host, where the electron and hole localise and recombine to emit light (Lawrence et al., 2012).

As can be deduced, there is noteworthy scientific scope for studying the detection capabilities of QDs as potential semiconductor nanosensors of ionising radiation in RMI applications. Nevertheless, despite the relevant scientific evidence, only some investigations have dealt with the application of QDs as ionising radiation sensors (Dai et al., 2002, Letant and Wang, 2006a, 2006b, Cevik et al., 2008, Waheed et al., 2009, Lawrence et al., 2012, Sahi and Chen, 2013) and even less (Baharin et al., 2010, Hobson et al., 2011, Lawrence et al., 2012, Valais et al., 2015) for potential uses in RMI. In the above consensus, this paper has focused on the radiation detection properties of Cadmium Selenide/Zinc Sulfide (CdSe/ZnS) core-shell type QDs for potential technological applications in X-ray radiology and for radiation safety monitoring e.g. in X-ray RMI installation rooms or in the natural radiation environment. The investigation was multidirectional in the sense that different experimental and computational techniques were utilised in order to explore possible factors which might affect the optical response of QDs after X-ray irradiation. The paper firstly reports various measurements and calculations of luminescence spectra after excitation of QDs by two types of ultraviolet (UV) lamps. The luminescence efficiency (LE) of different QD solutions is then reported, after their irradiation to X-rays generated by a diagnostic radiology RMI unit. Since the X-ray

irradiation employs several factors (high voltage generator, type, motion and status of the anode, collimator arrangements, filter, phototimers, general irradiation-handling electronic circuits (Doi, 2006) and the light detection is multilevel (photomultiplier tube, integration sphere, analog-to-digital converters, light-to-current measurement etc. (Michail et al., 2015c), advanced long-memory identifying techniques (Hurst, 1951, Hurst et al., 1965, Peng et al. 1992, 1993, 1994, 1995, 1998, Hu et al., 2001, Chen et al., 2002, Nikolopoulos et al., 2012, 2014a, 2014b, 2015, Petraki et al., 2013, Cantzos et al., 2015) were additionally employed, so as to trace any hidden long-lasting patterns in the optical emission time-series of the QDs after their X-ray irradiation. Additional signal analysis was performed in terms of Fourier and wavelet transforms to clarify the underlying physics in a more concise way.

## **2. Materials and methods**

### **2.1. Experimental procedures**

#### **2.1.1. Quantum Dot sample preparation**

The CdSe/ZnS QD samples were procured from Sigma-Aldrich (Lumidot 694622) dissolved in toluene. According to the manufacturer's specifications, the QD samples were of 4 nm particle size, extinction coefficient of  $1.6 \times 10^5 \text{ L} \cdot \text{mol}^{-1} \text{cm}^{-1}$ , density of 0.865 g/ml at 25<sup>0</sup>, excitation wavelength of 575 nm, emitting wavelength of 590 nm, full width at half

maximum lower than 40 nm and quantum yield greater than 30% (Lumidot, 2014). Note that the attenuation of light at a given wavelength is described by the extinction coefficient. The used CdSe/ZnS QD samples exhibited intermediate extinction coefficient values compared to a similar batch of QD samples of the same manufacturer series (Lumidot, 2014). QDs with smaller extinction coefficients (of the order of  $0.02 \times 10^5 \text{ L} \cdot \text{mol}^{-1} \text{cm}^{-1}$ ), typically emit light in the blue spectral band, that renders spectral incompatibilities with the available digital optical sensors, being usually sensitive to the red part of the spectrum. The QD samples were handled by inserting the solution into cubic  $12.5 \times 12.5 \times 45 \text{ mm}^3$  quartz cuvettes. To delineate the influence of the concentration in the radiation detection properties of the QD samples, their weight over volume (w/v) concentration was varied between three discrete values, viz.,  $14.2 \times 10^{-5} \text{ mg/mL}$ ,  $21.3 \times 10^{-5} \text{ mg/mL}$  and  $28.5 \times 10^{-5} \text{ mg/mL}$  respectively.

#### 2.1.2. UV excitation of the quantum dots

A number of factory-diluted QD solution-based samples were excited by UV radiation whilst their emission spectrum was detected and measured. Two different types of apparatus were employed for excitation and measurement, hereafter, denoted as Type I and Type II measurements.

Type I measurements were performed by an Ocean Optics S2000 grating monochromator (Ocean Optics Inc) (Valais et al., 2005) after excitation with a Vilber Lourmat, VL-215M,

312nm UV lamp. The light emitted by the excited QD samples was transferred to the spectrometer through an one metre long fiber optic cable (Avantes, Inc.FCB-UV400–2, Colorado, USA). Following a well tested methodology (Valais et al., 2005), the optical spectrum was collected with the UV lamp placed two centimetres away from the QD sample. Corrections for light signal degradation due to fiber optic light losses were taken into account.

Two modes were followed for the optical measurements of Type I: (a) Type A or transmission mode (tm), for which the apparatus measured the light from the rear side of the QD samples, namely the one that was not irradiated; (b) Type B or reflection mode (rm), for which the light fluence was measured, yet, at an angle of 45 degrees in respect to the cuvette's surface. Reflection mode simulates the back screen of ordinary conventional radiographic cassettes and the conventional mammographic cassettes (Valais et al., 2005). Transmission mode simulates all the other types of X-ray radiographic, fluoroscopic and computed tomography sensors (Valais et al., 2005). Since the quartz cuvettes that contain the QD samples may cause degradation of the optical photons that are emitted by these, two sets of independent repetitions of the experiments were conducted, however, the one set with empty cuvettes and the other set with cuvettes containing only the dissolver, namely cuvettes fully filled with toluene.

Type II measurements were conducted by a Perkin–Elmer UV–vis Lambda 15 Spectrophotometer (Perkin–Elmer Life And Analytical Sciences Inc., USA). This instrument has the ability to measure the light transmission of a sample after altering the wavelength of the UV excitation by a step of 0.1 nm in a range between 200 nm and 800



nm. To account for the potential degradation of the optical signal due to the quartz cuvette and possibly the toluene dissolver, a separate cuvette fully filled with toluene was placed besides the factory-diluted QD solution sample to allow for the automatic correction within the software which handled the operation of the Perkin–Elmer instrument.

### 2.1.3. X-ray irradiation of the quantum dots

The QD samples were exposed to X-rays generated by a Toshiba tube of a General Medical Merate radiography unit and a CPM 200 X-ray Generator. The tube was of rotating Tungsten anode, HVL 3.00 mm Al and total filtration 2.9 mm Al measured at 80 kVp. An additional 20 mm filtration was introduced in the beam to simulate the beam quality alternation that is induced by the human body (Kandarakis et al., 2005, Michail et al., 2014). The peak X-ray voltage varied between 50kVp to 130 kVp. The tube voltage was checked using a Piranha/RTI multifunction meter. A wide range of exposure times were employed from 200 ms to 2500 ms.

## 2.2. Mathematical aspects

### 2.2.1. Quantities related to the X-ray detection properties of the QDs.

#### 2.2.1.1. Absolute luminescence efficiency

The X-ray induced luminescence efficiency of a radiation sensor, can be calculated (Valais et al., 2005) according to equation (1):

$$\eta_{\Phi} = \frac{\dot{\Psi}_{\lambda}}{\dot{\Psi}_X} \quad (1)$$

where  $\dot{\Psi}_{\lambda}$  is the light energy flux emitted by a material after irradiation by X-rays and  $\dot{\Psi}_X$  is the X-ray energy flux impinging on the material's surface.

The X-ray energy flux,  $\dot{\Psi}_X$  of equation (1) necessitates the measurement of the X-ray energy spectrum impinging on the surface of the QD samples.

Thus, direct diagnostic X-ray spectra measurements were performed with a portable Amptek XR-100T X-ray spectrometer, based on a cadmium telluride (CdTe) crystal solid-state detector (Seferis et al., 2014). The detector was calibrated for energy scales, linearity checks and energy resolution, by using  $^{125}\text{I}$  and  $^{99\text{m}}\text{Tc}$   $\gamma$ -ray calibration sources (Michail et al., 2011, Martini et al., 2015). In order to minimize pile-up distortions, a dedicated

Tungsten spacer/collimation system (EXVC-W-Spacer) with thickness 36 mm and 300  $\mu\text{m}$  diameter) was used in order to stop and collimate X-rays greater than 100 keV. In addition the measured X-ray spectra were corrected for the efficiency of the CdTe detector.

The luminescence efficiency describes the radiation detection sensitivity of energy integrating sensors, namely the ones with output proportional to the total energy absorbed (Valais et al., 2005). Especially regarding the irradiation of a material with X-rays, the luminescence efficiency depends on the following intrinsic properties (Valais et al., 2005):

- (i) The total absorption efficiency, e.g., the fraction of the incident X-ray energy that is absorbed. This efficiency includes also the secondary X-ray photons, namely the K-fluorescence photons and the scattered X-ray radiation;
- (ii) The intrinsic conversion efficiency of X-ray radiation to optical light. This parameter expresses the fraction of the absorbed X-ray energy that is converted into light within the material;
- (iii) The light energy transmission efficiency. This parameter represents the fraction of the optical light that escapes from the material.

The luminescence efficiency can be alternatively defined as the ratio of the optical light energy over the incident X-ray energy (Valais et al., 2005).

The ratio of these quantities defines the absolute efficiency (AE) (Valais et al., 2005, Michail et al., 2014a) which is given by equation (2):

$$\eta_A = \frac{\dot{\Psi}_\lambda}{\dot{X}} \quad (2)$$

In equation (2), the X-ray energy flux  $\dot{\Psi}_x$  of equation (1) has been replaced by the incident exposure rate,  $\dot{X}$ . The latter can be easily experimentally determined through measurements with an ionisation chamber. Absolute efficiency is expressed in units of  $[\mu W \cdot m^{-2} / mR \cdot s^{-1}]$ , hereafter called Efficiency Units (E.U.).

Experimentally, the light energy flux ( $\dot{\Psi}_\lambda$ ) was measured with a well-calibrated setup (Valais et al., 2005, Michail et al., 2014a). The set-up comprised of a light integration sphere (Oriel 70451) coupled to a photomultiplier (EMI 9798B) with an S-20 photocathode (Fig.1). Note that the S-20 photocathode is of enhanced sensitivity (Valais et al., 2007). The output of the photomultiplier was then connected to an electrometer (Cary 401, vibrating reed type) operating in current mode (Valais et al., 2005). In this mode, the electrometer amplifies the electrical current of the photomultiplier which is a linear function of the total optical light emitted by the QD sample (Valais et al., 2005). An analogue to digital converter (ADC) was then employed to digitise the output of the electrometer. Finally, the ADC was connected to a computer to visualise the output in real-time and to store the data for further analysis. The incident exposure rate ( $\dot{X}$ ) was measured by a Radcal 2026C ionisation chamber dosimeter (Radcal Corp. USA). The AE was calculated from the time-series of the recorded electrical currents that were stored in the computer, according to well-established methodology (Valais et al., 2005).

### 2.2.1.2. Frequency Domain Properties of the Sensor Signal

In the frequency domain, a signal can be converted to its power spectral density (PSD),  $P(\omega)$ . For a discrete, random and stationary signal  $u(n)$  the PSD is given as:

$$P(\omega) = \lim_{N \rightarrow \infty} E[U(\omega)]^2 \quad (3)$$

where  $U(\omega)$  is the Discrete Time Fourier Transform (DTFT) of  $u(n)$ ,  $N$  its length and  $\omega$  is the angular frequency. In a practical scenario, in which the process  $u(n)$  is possibly nonstationary and for which only a finite duration segment is available, the signal is windowed with the window function  $w(n)$  of finite length  $N$  before applying the DTFT, i.e.:

$$U(\omega) = \sum_{n=0}^{N-1} w(n) \cdot u(n) \cdot e^{-j\omega n} \quad (4)$$

An estimate of the PSD is then given by Welch's averaged periodogram by computing the average power of  $M$  successive, overlapping windows of the signal  $u(n)$ . For the  $i^{\text{th}}$

window, the power is given as  $P_i(\omega) = |U_i(\omega)|^2$  with  $U_i(\omega)$  the DTFT of the  $i^{\text{th}}$  windowed signal. The averaged periodogram is then defined as:

$$P_w(\omega) = \frac{1}{M} \sum_{i=0}^{M-1} P_i(\omega) \quad (5)$$

Averaging the power over consecutive, overlapping windows effectively reduces the variance of the estimator of the PSD.

Computationally the PSD estimation was calculated for the light output of the QD samples for discrete windowed segments of the digitised time-series of the output of the electrometer. The calculation was implemented for a window length of 100 samples and a 50% overlap between the consecutive windowed segments. The window function selected was the Hamming window which is a typical choice for this method and provides good frequency resolution.

## 2.2.2. Quantities related to the long-memory of the whole measuring system.

### 2.2.2.1. Detrended Fluctuation Analysis (DFA)

Detrended Fluctuation Analysis is a method for scaling the long-range auto-correlation of

non-stationary, noisy or randomised signals and sometimes of short data length (Doi, 2006, Gupta et al., 2006, Ross et al., 2006, Yaffe et al., 2008, Kalyvas et al., 2011, Michail et al., 2014b). It is based on the quantification of the complexity of the signals. It is a modified root-mean-square analysis of a random walk based on the observation that a stationary time-series with long-range correlations can be integrated to form a self-similar process. Mean square distance of the signal from the local trend line is analysed as a function of a scale parameter and a power-law dependence is investigated. There is usually power-law dependence and interesting parameter is the exponent. In short, the original time-series is integrated once; then the fluctuations  $F(n)$  of the integrated signal are determined around the optimum least-square linear fit in a time window of size  $n$ . The slope of the line relating  $\log(F(n)) - \log(n)$  determines the scaling exponent (self-similarity parameter)  $b$ . This line may display a deflection (crossover) at a certain time scale where the slope abruptly changes. The interpretations of power-law scaling exponents and the crossovers are system dependent.

The DFA algorithm on 1-dimensional signal  $y_i$  ( $i = 1, \dots, N$ ), involves the following six steps (Peng et al. 1992, 1993, 1994, 1995, 1998; Petraki et al., 2013; Nikolopoulos et al., 2014a, 2015):

(i) In the first step, the integrated profile is determined:

$$y(k) = \sum_{i=1}^k (y(i) - \langle y \rangle) \quad (6)$$

where  $\langle \dots \rangle$  denotes the mean and  $k$  is the symbol of the different time scales.

(ii) The integrated signal,  $y(k)$ , is divided into non-overlapping bins of equal length,  $n$ .

(iii) In each bin of length  $n$ ,  $y(k)$  is fitted by using a polynomial function of order 1, which represents the trend in that box. A linear fit is usually used. The  $y$  coordinate of the fit line in each box is denoted by  $y_n(k)$ .

(iv) The integrated signal  $y(k)$  is detrended by subtracting the local trend,  $y_n(k)$ , in each

box of duration  $n$ . The detrended signal  $y_n^d(k)$  is hence calculated in each box as:

$$y_n^d(k) = y(k) - y_n(k) \quad (7)$$

(v) For a given bin size  $n$ , the root-mean-square (rms) fluctuations of the integrated and the detrended signal were calculated as:

$$F(n) = \sqrt{\frac{1}{N} \sum_{k=1}^N \left\{ \frac{y(k) - y_{\text{align}}}{n} \right\}^2} \quad (8)$$

Hence,  $F(n)$  represents the rms fluctuations of the detrended time-series  $y_n^d(k)$ .



(vi) The above is repeated for a broad range of scale box sizes  $(n)$  to provide a relationship between  $F(n)$  and the box size  $n$ . In general  $F(n)$  will increase with the size of segment  $n$ . Then a logarithmic graph ( $\log F(n)$  vs  $\log(n)$ ) is created. The linear dependence between the average root-mean square fluctuation  $F(n)$  and the bin size  $n$  indicates the presence of long-lasting self-fluctuations of the type:

$$F(n) \sim n^b \quad (9)$$

where, in the logarithmic graph, the linear slope is the scaling exponent  $b$  which quantifies the strength of the long-range correlations in the time-series.

For the calculations through the DFA algorithm, two different approaches were followed, namely (I) the sliding window technique and (II) the application in completely independent segments. The calculations were as follows:

- (I) To properly apply the sliding window technique the four discrete steps were followed:
  - (a) The signal was divided in segments-windows of certain size (number of samples). The employed sizes were between 16 and 64 samples (ms);
  - (b) In each segment-window the DFA algorithm was implemented;
  - (c) In each segment, the least square method was applied to the  $\log F(n)$ - $\log(n)$  linear representation of equation (9). Successive representations were considered those exhibiting squares of Spearman's correlation coefficient above 0.95;
  - (d) The window was advanced one sample and steps (a)-(c) were repeated until the end of

the signal was reached. Note that with these parameters, the analysis captures very fine variations of the digitised electrical signal in time at the expense of high computational cost as any given analysis window almost completely overlaps the preceding one. In this version of DFA only one slope was calculated, namely the scaling exponent was considered independent of scale. This slope was taken as the one representative for the scaling long-lasting trends of the light output of the irradiated QD samples. This one-slope DFA is the only choice for windows of lengths below 256 samples as the ones of the implementation of the sliding window technique.

(II) To calculate DFA in independent windows, after segmenting the digitised electrical signal to at least 256 samples (ms), the DFA algorithm was applied in each independent window. Then the  $\log F(n) - \log(n)$  linear representation of equation (9) was plotted through an interactive software designed for that purpose. A crossover was visually set as input to the software and then two different DFA slopes were calculated and plotted. Note, that this is the typical application of the DFA algorithm that was introduced by (Peng et al. 1992, 1993, 1994, 1995, 1998). Importantly, there were identified cases (Petraki et al., 2013) with three cross-overs, however this is not usual and for this reason it was not taken into account.

It is very important to note that the DFA technique can distinguish between the memory-differentiating signal's epochs (Peng et al. 1992, 1993, 1994, 1995, 1998; Petraki et al., 2013; Nikolopoulos et al., 2014a, 2015). Stationary background data are consistent with fractional Gaussian (fGn) modelling and exhibit DFA slopes between  $0 < b < 1$  (Petraki et

al., 2013, Nikolopoulos et al., 2014a, 2015). On the contrary, anomalous regions of strong memory present DFA slopes associated with modelling of fractional Brownian motion (fBm) are related to DFA slopes between  $1 < b < 2$  (Petraki et al., 2013, Nikolopoulos et al., 2014a, 2015).

#### 2.2.2.2. Hurst exponent

Hurst exponent (  $H$  ) is a mathematical quantity which can detect long-range dependencies in time-series (Stodilka et al., 2009, Lawrence et al., 2012). It can estimate the temporal smoothness of time-series and can search if the related phenomenon is a temporal fractal (Petraki et al., 2013; Nikolopoulos et al., 2012, 2014a,b, 2015).  $H$  -values between  $0.5 < H < 1$ , manifest long-term positive auto-correlation between samples in the time-series. This means that a high present value will be, possibly, followed by a high future value and this tendency will last for long future time-periods (persistence) (Petraki et al., 2013; Nikolopoulos et al., 2012, 2014a,b, 2015).  $H$  -values between  $0 < H < 0.5$  indicate time-series with long-term switching between high and low values. Namely, a high present value will be, possibly, followed by a low future value, whereas the next future value will be high and this switching will last long, into future (anti-persistence) (Petraki et al., 2013; Nikolopoulos et al., 2012, 2014a,b, 2015).  $H = 0.5$  implies completely uncorrelated time-series.

Hurst exponents were calculated from the calculated DFA scaling exponents  $b$  derived

from the analysis of the digitised time-series of the output of the electrometer. The relationship between the Hurst exponent and the DFA scaling exponent  $b$  differentiates in respect to the modelling of the time series and was calculated by (Petraki et al., 2013, Nikolopoulos et al., 2014a, 2015):

$$H = b - 1 \text{ for the fBm class } (1 < b < 2) \quad (10)$$

$$H = b \text{ for the fGn class } (0 < b < 1) \quad (11)$$

### 3. Results and discussion

Fig. 2 shows measured spectra produced by the X-ray tube, used in the present study. The tube settings ranged from 60 to 120 kVp at 63 mA and 2.5s. The system reproducibility was verified by measuring X-ray spectra several times.

Fig.3 presents the optical spectra of the Type I UV measurements. As aforementioned, this type of measurements refers to the UV excitation of the industrial QD samples in the transmission and reflection modes respectively. The emission optical spectrum of the VL-215M, UV lamp (no optical barrier) was degraded slightly in the region from 250 nm to 450 nm owing to the presence of an empty cuvette as the only optical barrier, in the transmission mode measurements (Fig3a). The output spectral response in Fig3a, implies that the presence of the cuvette used as the QD receptor, does not affect the incident spectrum of the VL-215M, UV lamp, within the visible wavelengths, when transmission

mode measurements are conducted. It was further observed in the transmission mode measurements, that the cuvettes being fully filled with pure toluene produced a spectrum with a slight shift to the right towards longer wavelengths but, significantly, without a noteworthy degradation of the normalised intensity of the optical signal. The significant difference was observed in the optical spectrum of the industrial (initial) QD samples (Fig 3a). In the optical range between 250 nm and 450 nm, the intensity of the industrial QD samples was significantly attenuated. Most importantly, the industrial QD samples exhibited an optical emission between 550 nm and 650 nm. The degradation in the range from 250 nm to 450 nm, cannot be attributed to the presence of the cuvette or the toluene, since both optical barriers did not alter the optical spectrum significantly in the transmission mode measurements. Under such perspective, it can be assumed that the pure QD gain medium of the industrial QD samples absorbs or scatters the light in the range between 250 nm to 450 nm. Since the observed optical light peak between 550 nm and 650 nm cannot be attributed to the lamp, toluene, cuvette or any combination of them, it can be due to the optical emission spectrum originated from the CdSe/ZnS QD nanocrystals of the QD samples. This view further implies that the QD nanocrystals of the industrial QD samples scatter the incident light in the region between 250 nm and 450 nm, more or less, because this region is out of their quantomechanic potentiality of absorption. It is worth to note that the optical peak between 550 nm and 650 nm from the transmission mode TypeI-Type A measurements coincides in full with the one given by (Hobson et al., 2011) and (Valais et al., 2015). This is reinforced by the findings of Fig. 3b. A pronounced peak can be observed in Fig.3b between 550 nm and 650 nm from the Type

I-Type B UV measurements for the optical spectral response of the QD samples. It is important that this was the only peak that was detected for the QD samples from the Type B UV measurements. This, in combination with the findings of Fig.3a, is a noteworthy indication that this peak can be attributed only to the nanocrystals of the QD samples. Hence, it can be deduced that the optical spectrum of the CdSe/ZnS QD nanocrystals of the QD samples is confined between 550 nm and 650 nm with a peak around 600 nm. It is worth to note that in Type B measurements the spectrum of the VL-215M, UV lamp was distinguished strongly from the one with an empty cuvette as the only optical barrier. The latter can be attributed to the scattering of the emitted UV light from the cuvette between 250 nm and 450 nm. This scattering is more pronounced when toluene is present in the cuvette, since the corresponding peak (red) of Fig.3a between 250 nm and 450 nm diminishes in Type B measurements.

The optical spectra of the measurements of Types A and B (Type I) are presented collectively in Fig. 4. The normalised intensity (N.I) values in the vertical axis of Figs 4a and 4b were calculated according to equation (12) from the corresponding ones of Figs 3a and 3b:

$$N.I. = N.I._{cuvette\ with\ QD\ sample} - (N.I._{no\ barrier} - N.I._{cuvette\ with\ pure\ toluene}) \quad (12)$$

The subscripts in (12) are the ones of the legend of Fig. 3. It is important that the calculation of equation (12) visualises a peak in the spectrum values between 550 nm and

650 nm for both types of measurements. In accordance to the argumentation given above, this peak corresponds to the emission spectrum of the CdSe/ZnS QD nanocrystals of the QD samples. It is worth to note that the calculation using equation (12) provides comparable values for the normalised spectrum within the above wavelength ranges, with the Type B spectrum giving slightly lower values. This could be attributed to scattering losses due to the 45 degree orientation of the optical fibre in the Type B UV measurements. The latter fact however is the most probable source of the significant differentiation of the Types A and B in the range between 250 nm and 450 nm. In the former case the normalised intensities were higher, whilst in the latter case, lower. In both cases, the variations of the normalised intensity values of Fig. 4 between 250 nm and 450 nm can be attributed to the presence of the solvent (toluene), the cuvette or both. Note, that this was the first time to address this type of alteration in the spectrum of the industrial Lumidot samples through similar methodology. The spectrum of Fig.5 shows the normalized transmittance spectrum of the CdSe/ZnS QD sample obtained with the Perkin–Elmer UV–vis Lambda 15 Spectrophotometer in the range between 200 nm and 800 nm. From Fig.5 a 70 nm wide transmission band, around 540 nm (green region), can be observed. After 630nm the transmittance reaches 100%. Fig.6 shows the normalised emission spectrum of the industrial Lumidot CdSe/ZnS samples as derived from Type B measurements confined to the optical wavelengths. Note, that the peak of Fig.6 is the focused clearest optical peak of Figs.4 and corresponds to the more pronounced one of Type I measurements.

As discussed in section 2.2.1.1, the absolute efficiency can be considered as an adequate

metric of the radiation detection ability of the CdSe/ZnS Lumidot QD gain matrix. Since, the light-induced electrical currents of the whole measuring apparatus are crucial for the estimation of the absolute efficiency (Kandarakis et al., 2005, Valais et al., 2007), it is of importance to address the overall divergences in the output time-series of the measuring set-up. Fig.7a presents a characteristic case of the deviation of the light-output of the whole set-up. Figs. 7b and 7c present the characteristic outputs of the method of DFA, though via application of the technique I of section 2.2.2.1, namely the sliding window technique. Fig.7d depicts the wavelet scalogram of Fig7a. At first, it should be emphasised that this measurement was derived after exciting the QD samples of the concentration of  $28.5 \times 10^{-5}$  mg/mL with medical X-rays for 2500 ms. As can be observed from Fig.7a, the X-rays ionised the QD samples, since light was produced during their excitation. However the time series of the electrical currents that were digitised by the ADC of the set-up, presented intense variations up to 1000 ms and from 3000 ms and after. Note that the start of the excitation was at the instance of 480 ms with respect to the measurement time of the ADC circuit. Although the excitation time was 2500 ms the light output of the excited QD sample converted to digitised electrical current, still remained after the expected end, viz. after 2980 ms. This after-exposure effect, could be attributed to the whole measurement set-up, namely the X-ray unit, the excited QD sample and the light-measuring system (integration sphere, photomultiplier, vibrating reed electrometer). Note that according to other investigators (Baharin et al., 2010, Hobson et al., 2011) the QDs are expected to respond very quickly, however, this cannot be ascertained by the results of Fig.7c, since these data correspond to electrometer readings (giving light energy flux) and not to decay



time specific measurements, which are required to estimate the time response of a scintillator (Seferis and Zych 2016, Seferis et al., 2016). The findings of Fig.7a are strongly reinforced by the results of the DFA outputs (Figs.7b and 7c). Between the excitation start and approximately at 800 ms, the DFA scaling exponent  $b$  (DFA slope, section 2.2.2.1.) exhibited a significant increase above 1 with several values being well above 1.5 (Fig.7c). As explained in section 2.2.2.1 and according to several related publications (Hurst, 1951, Hurst et al., 1965, Peng et al. 1992, 1993, 1994, 1995, 1998, Hu et al., 2001, Chen et al., 2002, Nikolopoulos et al., 2012, 2014a, 2014b, 2015, Petraki et al., 2013, Cantzos et al., 2015), DFA slopes above one are strongly associated with the fBm class. Note that according to related publications (Nikolopoulos et al., 2012, 2014a, 2014b, 2015, Petraki et al., 2013, Cantzos et al., 2015), the fBm class implies that there were hidden long-memory trends in the time series. The fact that the DFA scaling exponent  $b$  increased above the cut-off limit of 1.5, implies strong fBm behaviour well away from the randomness of the fGn class (Nikolopoulos et al., 2012, 2014a, 2014b, 2015, Petraki et al., 2013, Cantzos et al., 2015). Note that the fBm class is the well-established class of long-range interactions. In the above consensus and accounting several related publications (Nikolopoulos et al., 2012, 2014a, 2014b, 2015, Petraki et al., 2013, Cantzos et al., 2015), between 500 ms and 800 ms (Figs.7a and 7c), each value of the electrical currents that had been induced by the X-ray excitation of the QD samples, associated with its past and future values in a chaotic deterministic regime; an instant value of the electrical current was determined by one or more previous values (past of the system) and determined the forthcoming values (future of the system) in a chaotic manner (Nikolopoulos et al., 2012, 2014a, 2014b, 2015, Petraki

et al., 2013, Cantzos et al., 2015). In general, during this regime, small disruptions could lead the system out of equilibrium in the sense of forecasting the presence of the system from its past (Nikolopoulos et al., 2012, 2014a, 2014b, 2015, Petraki et al., 2013, Cantzos et al., 2015). The QD emitting system of Fig.7 operated, hence under a predictable, chaotic regime. This regime extended up to the 800 ms where the system came back to equilibrium. Between 1000 ms and 3000 ms, the DFA scaling exponent  $b$  was of the order of 1 or below. This is well correlated with randomness and the lack of memory effects (Peng et al. 1992, 1993, 1994, 1995, 1998). During this period the light emitted by the QD samples and recorded by the whole measurement set-up had random stochastic nature. This finding is in agreement with the well-known stochastic behaviour of the interaction of ionising radiation with matter. This stochastic regime implies also that, if the X-ray irradiation could last very long, the QD nanosensory system would exhibit a rather stable light and digitised electrical output and the corresponding electrical current time-series would be stochastic, namely described under the randomness of the fGn class. During this stochastic regime the QD system can be modelled with probabilistic methods, for example through Monte Carlo simulation. It is this principal probabilistic nature that intensifies the results of the fBm segments as well, where long-memory is addressed and in which the QD system is deterministic from the chaotic point of view. The chaotic long-memory regime is addressed once more after the end of the X-ray excitation and, importantly at a greater time extend compared to the one of the beginning of the excitation. It is significant to note, that the measured ripple factor of 2 of the employed X-ray unit could not explain, in single, these results, nor can the vibration physics of the electrometer's reed. Hence, the long-

memory fBm behaviour of the QDs can be attributed to the measurement apparatus on the whole. It is also of significance that the wavelet scalogram of the Fig.7d verified the high power areas in the same segments as those observed by the DFA method. Note, that the method employed in the generation of Fig.7d is completely different from the one of Fig.7b. Yet both methods had clearly identified the two areas with the chaotic long-memory regimes. Some noteworthy spikes in the DFA exponent after 3500 ms from the start of the excitation are of no scientific value, because they were associated with a significant decrease in the square of the Spearman's correlation coefficient. Under another viewpoint, the Hurst exponents of the long-memory chaotic regimes ranged within  $0.5 < H < 1$  ( $1.5 < b < 2$ ) for the identified fBm classes. Some scaling exponents above 2 ( $b > 2$ ) can be tied (Chen et al., 2006, Kinsner, 2007, D'Addio et al., 2013) to Hurst exponents saturated to  $H = 1$ . The Hurst exponents above 0.5 up to 1 can be associated with persistency. Most pronounced were the effects for Hurst exponents above 0.7 and up to 1 ( $1.7 < b < 2$ ). Within this chaotic long-memory regime of the digitised light output of the X-ray excited QD samples, the Hurst exponents were strongly persistent. This means that if the digitised light output increased in one time interval, it continued to increase (Nikolopoulos et al., 2012, 2014a, 2014b, 2015, Petraki et al., 2013, Cantzos et al., 2015) (e.g. the regime between the excitation start and approximately 800 ms after). In another interpretation, if the signal decreased in a certain period, it was most probable to continue decreasing (Nikolopoulos et al., 2012, 2014a, 2014b, 2015, Petraki et al., 2013, Cantzos et al., 2015) (e.g. the regime after 3000 ms). All the above key findings are also verified by the data shown in Figs 8. Indeed, for the contoured windows of Fig.8b (long-memory

chaotic segments identified in Fig.7), the corresponding DFA scatter plots according to the technique II of section 2.2.2.1 (Figs 8d and 8e), showed that the long-range DFA scaling slopes  $b$  were approximately 1.95 (legends of Figs 8d and 8e). According to the data of section 2.2.2.1, these areas are characterised as fBm and are associated with persistent Hurst exponents (equation 10) of about 0.95. On the contrary, the non-contoured segment was an fGn segment according to the data of Fig.8e, since both DFA slopes were below 1. According to equation (11) these segments were related to a persistent random stochastic fGn class (Petraki et al., 2013). Following an alternative interpretation, the sliding window DFA method (technique I, section 2.2.2.1) and the wavelet scalogram can assist in identifying the random fGn segments of the light output of the measuring system. Such areas (e.g. between 1000 ms and 2500 ms) are adequate for the analysis of the electrical current time series that are produced by the light that the QDs emit when excited by X-rays. This approach was finally implemented from a computational point of view, so as to determine the random segments of the electrical signals for the calculation of the absolute efficiency according to equation (2) and the references (Kandarakis et al., 2005, Valais, et al., 2005, Michail et al., 2014). The durations of the useful fGn segments according to the above approach, ranged between 80 and 2000 samples and led to sufficient numbers of sample to achieve accuracy in the 95% significance level. It is also important that the random fGn segments did not show differentiations in their Fourier averaged periodogram profiles as the ones depicted in Fig.9 Despite that Fig.9 is an example case, the remaining data exhibited similar averaged periodogram profiles. For the estimations of Fig.9, as aforementioned, a window length of 100 samples was selected with a 50% overlap

between consecutive windowed segments. As mentioned in section 2.2.1.2, the selected window function was the Hamming window which is a typical choice for this method and provides good frequency resolution. From the data of Fig.9 it can be deduced that the electrical signals for the X-ray excited QD samples did not show any special periodic behaviour from the Fourier transform point of view. This viewpoint proposes an alternative interpretation of the randomness of the fGn segments, since no special Fourier enhancement can be related with low varying fGn background (Petraki et al., 2013). Fig.10 presents the corresponding results for the estimation of the absolute efficiency from the fGn segments of the electrical current time-series. The errors in Fig.10 were estimated from the standard deviation of each random fGn data set at the 95% confidence intervals. It is important to note that the above methodological approach excluded non-fGn data from the analysis.

The curves of the absolute efficiency data shown in Fig.10 were derived through nonlinear fits to polynomial functions. The curve for the 14.2 mg/mL concentration corresponds to the polynomial quadratic function ( $y = a + b \cdot x + c \cdot x^2 + d \cdot x^3 + e \cdot x^4$ ), whilst the other two

curves correspond to the function  $y = \frac{(a + b \cdot \log(x))}{(1 - c \cdot \log(x) + d \cdot (\log(x))^2)}$ . The comparison of the

fitted of the data depicted in Fig.10 clearly demonstrates that the investigated QD samples can detect the X-rays within the RMI energy range. This finding is in agreement with the work of other investigators (Del Sordo et al., 2009, Stodilka et al., 2009, Baharin et al., 2010, Hobson et al., 2011). It is important that this paper was the first one in which a variety of methods has been introduced and compared to understand the underlying

mechanisms of the X-ray induced emission of the Lumidot QD system, focusing on the differences of their acquisition and detection ability. Moreover, it was also the first time to address the differences in the detection efficiency when different QD solutions are employed. The findings of this paper revealed that the higher concentration sample (28.4 mg/mL) exhibited its maximum absolute efficiency value at 80 kVp tube voltage. From Fig. 10 can be also shown that the AE of the QD solutions of higher concentration, dropped milder compared to the corresponding drop of the AE of the lower concentration samples. It can be observed, as well, that the peak of the absolute efficiency values of the samples of low solution concentration is shifted to higher X-ray tube voltages.

It should be noted, that the absolute efficiency data refer to different solutions contained in cuvettes of certain thickness and not to solutions or sensors of different thickness values. This differentiation could explain the low absolute efficiency values of this paper in comparison to the ones of other related papers (Michail et al., 2013). Yet, this paper reported a new approach for the investigation of the luminescence process of the CdSe/ZnS QDs after irradiation by RMI X-rays. Several design parameters should be addressed for the optimisation of the investigated QD nanosensory system, as well as for a future utilisation in the medical praxis. These issues are, however, beyond of the scope of this paper and will be investigated in future work.

#### **4. Conclusions**

An investigation of luminescence and radiation detection properties of the CdSe/ZnS quantum dot nanocrystals has been presented. The work focused on the luminescence of

the CdSe/ZnS quantum dots after their excitation by UV radiation and medical X-rays. The scope was to explore the possible factors and mechanisms which might affect the optical response of the quantum dots after their X-ray irradiation. In a multidirectional approach, several experimental and computational techniques were utilised jointly with the detrended fluctuation analysis method and the Hurst exponent, to identify, on the basis of deterministic chaos theory, hidden long-memory trends in the measured, X-ray induced, luminescence signals. Employing these approaches, long-lasting segments of fractional Brownian motion were extracted from the stationary segments following the fractional Gaussian noise process associated with the stochastic nature of the interaction between medical X-rays and the investigated quantum dots. Additional signal analysis was also performed in terms of the Fourier and wavelet transforms. The results revealed that the UV induced emission spectrum of the CdSe/ZnS shows a symmetrical peak between 450 nm and 650 nm with highest intensity around 550 nm. Significant discrepancies were observed in the UV induced spectra between 250 nm and 450 nm via two different types of UV lamps. These discrepancies were attributed to the presence of the solvent, the cuvette or both. The absolute luminescence efficiency calculated from the random segments, of the fractional Gaussian class, showed variations. The Fourier analysis of the digitized electrical signals of the X-ray excited QD solutions did not show any special periodic behaviour between the different solutions indicating non-specific enhancement in the segments analysed with long-memory techniques. The absolute efficiency of the solution samples of the higher concentrations was higher compared to the one of the samples with lower concentrations, but only up to 80 kVp tube voltage. The absolute efficiency of the

highly concentrated QD solutions decreased slightly with respect to the samples with lower concentrations. The results demonstrated that the CdSe/ZnS quantum dot has great potential for detection of X-rays within the energy range suitable to medical imaging applications.

### **Acknowledgements**

Authors would like to acknowledge the assistance of Miss Vaia Koukou and Miss Niki Martini for the support on the direct X-ray spectra measurements. Authors Ioannis Valais, Christos Michail and Christina Fountzoula wish also to thank the Special Account for Research Grants of the TEI of Athens, in the framework of the Internal Programme for the Support of the TEI of Athens Researchers, for 2015, code 80224 for the financial support of this research.

### **References**

- Assadi M., Afrasiabi K., Nabipour I., Seyedabadi M., 2011. Nanotechnology and nuclear medicine; research and preclinical applications. *Hell. J. Nucl. Med.* 14(2), 149-159.
- Baharin, R., Hobson, P., Smith, D., 2010. Simulation of MeV electron energy deposition in CdS quantum dots absorbed in silicate glass for radiation dosimetry. *J. Phys.: Conf. Ser.* 245, 012007.
- Beierholm, A., Andersen, C., Lindvold, L., Kjær-Kristoffersen, F., Medin, J., 2008. A comparison of BCF-12 organic scintillators and Al<sub>2</sub>O<sub>3</sub>:C crystals for real-time medical dosimetry. *Radiat. Meas.* 43(2-6), 898-903.



- Blasse, G., Grabmaier, B., 1994. Luminescent materials. Springer, Berlin.
- Cantzos, D., Nikolopoulos, D., Petraki, E., Nomicos, C., Yannakopoulos, P., Kottou, S., 2015. Identifying long-memory trends in pre-seismic MHz Disturbances through Support Vector Machines. J. Earth. Sci. Clim. Change. 6(263), 1-9.
- Cevik, U., Bacaksiz, E., Damla, N., Celik, A., 2008. Effective atomic numbers and electron densities for CdSe and CdTe semiconductors. Radiat. Meas. 43, 1437-1442.
- Chen, Z., Ivanov, P., Hu, K., Stanley, H., 2002. Effect of non-stationarities on detrended fluctuation analysis. Phys. Rev. E. 65(4), 041107.
- Chen, C., Wang, W., Chang, Y., Wu, Y., Lee, Y., 2006. A correlation between the b-value and the fractal dimension from the aftershock sequence of the 1999 Chi-Chi, Taiwan, earthquake. Geophys. J. Int. 167, 1215-1219.
- D'Addio, G., Accardo, A., Fornasa, E., Cesarelli, M., De Felice, A., 2013. Fractal Behaviour of Heart Rate Variability Reflects Abnormal Respiration Patterns in OSAS Patients. IEEE Comput. Cardiol. Conf. 40, 445-448.
- Dai, S., Saengkerdsub, S., Im, H., Stephan, A., Mahurin, S., 2002. Nanocrystal-based scintillators for radiation detection. AIP Conf. Proc. 632, 220-224.
- David, S., Michail, C., Seferis, I., Valais, I., Fountos, G., Liaparinis, P., Kandarakis, I., Kalyvas, N., 2016. Evaluation of  $\text{Gd}_2\text{O}_2\text{S:Pr}$  granular phosphor properties for X-ray mammography imaging J. Lumin. 169, 706-710.
- Del Sordo, S., Abbene, L., Caroli, E., Mancini, A., Zappettini, A., Ubertini, P., 2009. Progress in the Development of CdTe and CdZnTe Semiconductor Radiation Detectors for Astrophysical and Medical Applications. Sensors 9, 3491-3526.
- Doi, K., 2006. Diagnostic imaging over the last 50 years: research and development in medical imaging

- science and technology. Phys. Med. Biol. 51, R5-R27.
- Eychmuller, A., 2000. Structure and photophysics of semiconductor nanocrystals. J. Phys. Chem. B 104, 6514-6528.
- Goncharova, O., Kalinov, V., Voitovich, A., 2004. The energy transfer in irradiated dielectric thin film structures with CdS and CdSe nanocrystals. Radiat. Meas. 38, 775-779.
- Gbur, T., Vlk, M., Cuba, V., Beitlerova, A., Nikl, M., 2013. Preparation and luminescent properties of ZnO:Ga(La)/polymer nanocomposite. Radiat. Meas. 56, 102-106.
- Guo, S., Konopny, L., Popovitz-Biro, R., Cohen, H., Sirota, M., Lifshitz, E., Lahav, M., 2000. Topotactic Release of CdS and Cd<sub>1-x</sub>MnxS from Solid Thioalkanoates with Ammonia to Yield Quantum Particles Arranged in Layers within an Organic Composite. Adv. Mater. 12, 302-306.
- Gupta, R., Grasruck, M., Suess, C., Bartling, S., Schmidt, B., Stierstorfer, K., Popescu, S., Brady, T., Flohr, T., 2006. Ultra-high resolution flat-panel volume CT: fundamental principles, design architecture, and system characterization. Eur. Radiol. 16, 1191-1205.
- Hobson, P., Leslie, D., Smith, D., 2011. Effect of Gamma Radiation on Potential Ionising Radiation Detectors and Dosimeters based on Quantum Dots. IEEE Nucl. Sci. Conf. Proc., MIC12.M-115.
- Hu, K., Ivanov, P., Chen, Z., Carpena, P., Stanley, H. 2001. Effect of trends on detrended fluctuation analysis. Phys. Rev. E. 64, 011114.
- Hurst, H., 1951. Long Term Storage Capacity of Reservoirs. T. Am. Soc. Civ. Eng. 116, 770-799.
- Hurst, H., Black, R., Simaiki, Y., 1965. Long-term storage: an experimental study. Constable, London.
- Jacobsohn, L., Bennett, B., Muenchausen, R., Smith, J., Wayne Cooke, D., 2007. Luminescent properties of nanophosphors. Radiat. Meas. 42, 675-678.
- Kalyvas, N., Liaparinos, P., Michail, C., David, S., Fountos, G., Wójtowicz, M., Zych, E., Kandarakis, I., 2011. Studying the luminescence efficiency of Lu<sub>2</sub>O<sub>3</sub>:Eu nanophosphor material for digital X-ray

- imaging applications. *App. Phys. A.* 106(1), 131-136.
- Kandarakis, I., Cavouras, D., 2001. Modeling the effect of light generation and light attenuation properties on the performance of phosphors used in medical imaging radiation detectors. *Nucl. Instr. and Meth. Phys. Res. A* 460, 412-423.
- Kandarakis, I., Cavouras, D., Nikolopoulos, D., Anastasiou, A., Dimitropoulos, N., Kalivas, N., Ventouras, E., Kalatzis, I., Nomicos, C., Panayiotakis, G., 2005. Evaluation of ZnS:Cu phosphor as X-ray to light converter under mammographic conditions. *Radiat. Meas.* 39, 263-275.
- Kim, S., Park, J., Kang, S., Cha, B., Cho, S., Shin, J., Son, D., Nam, S. 2007. Investigation of the imaging characteristics of the Gd<sub>2</sub>O<sub>3</sub>:Eu nanophosphor for high-resolution digital X-ray imaging. *Nucl. Instrum. Meth. Phys. Res. A.* 576, 70-74.
- Kinsner, W., 2007. Unified Approach To Fractal Dimensions. *International Journal of Cognitive Informatics and Natural Intelligence.* 1(4), 26-46.
- Klassen, N., Kedrov, V., Ossipyan, Y., Shmurak, S., Shmytko, I., Krivko, O., Kudrenko, E., Kurlov, V., Kobelev, N., Kiselev, A., Bozho, S. 2009. Nanoscintillators for Microscopic Diagnostics of Biological and Medical Objects and Medical Therapy. *IEEE Trans. Nanobioscience.* 81, 20-32.
- Knoll, G., 2010. *Radiation Detection and Measurement.* John Willey and Sons, Washington DC.
- Kobayashi, M., Aogaki, S., Takeutchi, F., Tamagawa, Y., Usuki, Y., 2012. Performance of thin long scintillator strips of GSO:Ce, LGSO:Ce and LuAG:Pr for low energy  $\gamma$ -rays. *Nucl. Instr. and Meth. Phys. Res. A* 693, 226-235.
- Konstantatos, G., Clifford, J., Levina, L., Sargent, E. 2007. Sensitive solution-processed visible-wavelength photodetectors. *Nat. Photonics* 1(9), 531-534.
- Konstantatos, G., Sargent, E., 2011. Colloidal quantum dot photodetectors. *Infrared Phys. Tech.* 54(3), 278-282.

- Krasnyj, J., W. Donderowicz, W. Jacak, M. Tytus 2007. Photoluminescence structure of highly excited quantum dots of type II. *Radiat. Meas.* 42, 683-687.
- Lawrence, W., Thacker, S., Palamakumbura, S., Riley, K., Nagarkar, V., 2012. Quantum Dot-Organic Polymer Composite Materials for Radiation Detection and Imaging. *IEEE Trans. Nucl. Sci.* 59(1), 215-221.
- Letant, S., Wang, T., 2006. Semiconductor Quantum Dot Scintillation under Gamma Ray Irradiation. *Nano Lett.* 6(12), 2877-2880.
- Letant, S., Wang, T., 2006. Study of porous glass doped with quantum dots or laser dyes under alpha irradiation. *Appl. Phys. Lett.* 88(10), 103110.
- Lumidot 2014 CdSe/ZnS 610 core-shell type quantum dots, specification sheet, 694614 Sigma-Aldrich, <http://www.sigmaaldrich.com/catalog/product/aldrich/694614?lang=en&region=GR>
- Ma, Y., Qi, L., Ma, J., Cheng, H., Shen, W., 2003. Synthesis of Submicrometer-Sized CdS Hollow Spheres in Aqueous Solutions of a Triblock Copolymer. *Langmuir* 19, 9079-9085.
- Malyukin, Y., 2010. Fundamental aspects of activated nanocrystal luminescence and possible applications. *Radiat. Meas.* 45, 589-593.
- Martini, N., Koukou, V., Michail, C., Sotiropoulou, P., Kalyvas, N., Kandarakis, I., Nikiforidis G., and Fountos, G., 2015. Pencil beam spectral measurements of Ce, Ho, Yb and Ba powders for potential use in Medical applications. *Journal of Spectroscopy* 2015, 563763.
- Michail, C., David, S., Liaparinos, P., Valais, I., Nikolopoulos, D., Kalivas, N., Toutountzis, A., Sianoudis, I., Cavouras, D., Dimitropoulos, N., Nomicos, C., Kourkoutas, K., Kandarakis, I., Panayiotakis, G., 2007. Evaluation of the imaging performance of LSO powder scintillator for use in X-ray mammography *Nucl. Instr. and Meth. Phys. Res. A* 580, 558-561.
- Michail, C., Fountos, G., Valais, I., Kalyvas, N., Liaparinos, P., Kandarakis, I., Panayiotakis, G., 2011.

- Evaluation of the red emitting  $\text{Gd}_2\text{O}_2\text{S}:\text{Eu}$  powder scintillator for use in indirect X-ray digital mammography detectors. IEEE Trans. Nucl. Sci. 58, 2503-2511.
- Michail, C., Kalyvas, N., Valais, I., David, S., Seferis, I., Toutountzis, A., Karabotsos, A., Liaparinis, P., Fountos, G., Kandarakis, I., 2013. On the response of  $\text{GdAlO}_3:\text{Ce}$  powder scintillators, J Lumin. 144, 45-52.
- Michail, C., Valais, I., Seferis, I., Kalyvas, N., David, S., Fountos, G., Kandarakis, I., 2014. Measurement of the luminescence properties of  $\text{Gd}_2\text{O}_2\text{S}:\text{Pr,Ce,F}$  powder scintillators under X-ray radiation. Radiat. Meas. 70, 59-64.
- Michail, C., Kalyvas, N., Valais, I., Fudos, I., Fountos, G., Dimitropoulos, N., Koulouras, G., Kandris, D., Samarakou, M., Kandarakis, I., 2014. Figure of Image Quality and Information Capacity in Digital Mammography. BioMed. Res. Int. 2014, 634856.
- Michail, C., Valais, I., Seferis, I., Kalyvas, N., Fountos, G., Kandarakis, I. 2015. Experimental measurement of a high resolution CMOS detector coupled to CsI scintillators under X-ray radiation. Radiat. Meas. 74, 39-46.
- Michail, C., 2015. Image Quality Assessment of a CMOS/ $\text{Gd}_2\text{O}_2\text{S}:\text{Pr,Ce,F}$  X-ray Sensor. Journal of Sensors. 2015, 874637.
- Michail, C., David, S., Bakas, A., Kalyvas, N., Fountos, G., Kandarakis, I., Valais, I., 2015. Luminescence Efficiency of  $(\text{Lu,Gd})_2\text{SiO}_5:\text{Ce}$  (LGSO:Ce) crystals under X-ray radiation. Radiat. Meas. 80, 1-9.
- Nikolopoulos, D., Petraki, E., Marousaki, A., Potirakis, S., Koulouras, G., Nomicos, C., Panagiotaras, D., Stonham, J., Louizi, A., 2012. Environmental monitoring of radon in soil during a very seismically active period occurred in South West Greece. Journal of Environmental Monitoring, 14, 564-578.
- Nikolopoulos, D., Petraki, E., Vogiannis, E., Chaldeos, Y., Yannakopoulos, P., Kottou, S., Nomicos, C., Stonham, J., 2014a. Traces of self-organisation and long-range memory in variations of environmental radon in soil: Comparative results from monitoring in Lesvos Island and Ileia (Greece). J. Radioanal.

Nucl. Chem. 299, 203-219.

Nikolopoulos, D., Petraki, E., Temenos, N., Kottou, S., Koulougliotis, D., Yannakopoulos, P., 2014<sup>b</sup>. Hurst exponent analysis of indoor radon profiles of Greek apartment dwellings. *J. Phys. Chem. Biophys.* 4(6), 1-8.

Nikolopoulos, D., Petraki, E., Nomicos, C., Koulouras, G., Kottou, S., Yannakopoulos, P., 2015. Long-memory trends in disturbances of radon in soil prior to the twin ML=5.1 earthquakes of 17 November 2014 Greece. *J. Earth Sci. Clim. Change.* 6(1), 1-10.

Nistor, S., Stefan, M., Ghica, D., Nistor, L., 2013. Nanosize induced effects in luminescent ZnS:Mn. *Radiat. Meas.* 56, 40-43.

Pang, L., Shen, Y., Tetz, K., Fainman, Y., 2005. PMMA quantum dots composites fabricated via use of pre-polymerization. *Opt. Express.* 13(1), 44-49.

Peng, C., Buldyrev, S., Goldberger, A., Havlin, S., Sciortino, F., Simons, M., Stanley, H., 1992. Long-range correlations in nucleotide sequences. *Nature.* 356, 168-70.

Peng, C., Mietus, J., Havlin, S., Stanley, H., Goldberger, A., 1993. Long Range Anti-correlations and Non-Gaussian Behavior of the Heartbeat. *Phys. Rev. Lett.* 70(9), 1343-1346.

Peng, C., Buldyrev, S., Havlin, S., Simons, M., Stanley, H., Goldberger, A., 1994. Mosaic organization of DNA nucleotides. *Phys. Rev. E.* 49, 1685-1689.

Peng, C., Havlin, S., Stanley, H., Goldberger, A. 1995. Quantification of scaling exponents and crossover phenomena in non-stationary heartbeat time series. *Chaos.* 5(1), 82-87.

Peng, C., Hausdorff, J., Havlin, S., Mietus, J., Stanley, H., Goldberger, A., 1998. Multiple-time scales analysis of physiological time series under neural control. *Physica A.* 249, 491-500.

Petraki, E., Nikolopoulos, D., Fotopoulos, A., Panagiotaras, D., Koulouras, G., Zisos, A., Nomicos, C., Louizi, A., Stonham, J., 2013. Self-organised critical features in soil radon and MHz electromagnetic

- disturbances: Results from environmental monitoring in Greece. *Appl. Radiat. Isotop.* 72, 39-53.
- Prochazkova, L., Cuba, V., Mrazek, J., Beitlerov, A., Jary, V., Nikl, M., 2016. Preparation of Zn(Cd)O:Ga-SiO<sub>2</sub> composite scintillating materials. *Radiat. Meas.* 1-5.
- Rauch, T., Böberl, M., Tedde, S., Fürst, J., Kovalenko, M., Hesser, G., Lemmer, U., Heiss, W., Hayden, O., 2009. Near-infrared imaging with quantum-dot-sensitized organic photodiodes. *Nat. Photonics* 3, 332-336.
- Rodnyi, P., 2001. Progress in fast scintillators. *Radiat. Meas.* 33, 605-614.
- Ross, W., Cody, D., Hazle, J., 2006. Design and performance characteristics of a digital flat-panel computed tomography system. *Med. Phys.* 33, 1888-1901.
- Sahi, S., Chen, W., 2013. Luminescence enhancement in CeF/ZnO nanocomposites for radiation detection. *Radiat. Meas.* 59, 139-143.
- Seferis, I., Michail, C., Valais, I., Fountos, G., Kalyvas, N., Stromatia, F., Oikonomou, G., Kandarakis, I., Panayiotakis, G., 2013. On the response of a europium doped phosphor-coated CMOS digital imaging detector. *Nucl. Instr. and Meth. Phys. Res. A* 729(21), 307-315.
- Seferis, I., Michail, C., Valais, I., Zeler, J., Liaparinos, P., Fountos, G., Kalyvas, N., David, S., Stromatia, F., Zych, E., Kandarakis, I., Panayiotakis, G., 2014. Light emission efficiency and imaging performance of Lu<sub>2</sub>O<sub>3</sub>:Eu nanophosphor under X-ray radiography conditions: Comparison with Gd<sub>2</sub>O<sub>2</sub>S:Eu. *J. Lumin.* 151, 229-234.
- Seferis, I., Zeler, J., Michail, C., Valais, I., Fountos, G., Kalyvas, N., Bakas, A., Kandarakis, I., Zych, E., 2015. Preparation and imaging performance of nanoparticulated LuPO<sub>4</sub>:Eu semitransparent films under x-ray radiation, *Proc. SPIE* 9668, *SPIE Micro+Nano Materials, Devices, and Systems*, 96682H.
- Seferis, I., Zych, E., 2016. On the synthesis of LuAG:Ce fine powders by molten salts methods and spectroscopic properties of the products. *J. Lumin.* 169, 838-843.

- Seferis, I., Zeler, J., Michail, C., Valais, I., Fountos, G., Kalyvas, N., Bakas, A., Kandarakis, I., Zych, E., 2016. On the response of semitransparent nanoparticulated films of  $\text{LuPO}_4\text{:Eu}$  in polyenergetic X-ray imaging applications. *Appl. Phys. A*. 122:526.
- Stodilka, R., Carson, J., Kui, Y., Zaman, M., Li, C., Wilkinson, D. 2009. Optical Degradation of  $\text{CdSe/ZnS}$  Quantum Dots upon Gamma-Ray Irradiation. *J. Phys. Chem. C*. 113, 2580-2585.
- Valais, I., Kandarakis, I., Nikolopoulos, D., Sianoudis, I., Dimitropoulos, N., Cavouras, D., Nomicos, C., Panayiotakis, G., 2005. Luminescence Efficiency of  $\text{Gd}_2\text{SiO}_5\text{:Ce}$  Scintillator Under X-Ray Excitation. *IEEE Trans. Nucl. Sci.* 52(5), 1830-1835.
- Valais, I., Michail, C., David, S., Liaparinos, P., Fountos, G., Paschalis, T., Kandarakis, I., Panayiotakis, G., 2010. Comparative Investigation of  $\text{Ce}^{3+}$  doped Scintillators in a wide Range of Photon Energies covering X-ray CT, Nuclear Medicine and Megavoltage Radiation Therapy Portal Imaging applications. *IEEE Trans. Nucl. Sci.* 57(1), 3-7.
- Valais, I., Michail, C., Nikolopoulos, D., Fountzoula, C., Bakas, A., Yannakopoulos, P., Fountos, G., Panayiotakis, G., Kandarakis, I., 2015. Effect of the Concentration on the X-ray Luminescence Efficiency of a Cadmium Selenide/Zinc Sulfide ( $\text{CdSe/ZnS}$ ) Quantum Dot Nanoparticle Solution. *J. Phys. Conf. Ser.* 637, 012031.
- Van Eijk, C., W., 2008. Radiation detector developments in medical applications: inorganic scintillators in positron emission tomography. *Radiat. Prot. Dosim.* 129, 13-21.
- Voitenko, I., Muth, J., Gerhold, M., Cui, D., Xu, J., 2007. Tunable photoluminescence of polymer doped with  $\text{PbSe}$  quantum dots. *Mater. Sci. Eng. C*. 27, 1078-1081.
- Waheed, A., Forsyth, D., Watts, A., Saad, A., Mitchell, G., Farmer, M., Harris, P., 2009. The track nanotechnology. *Radiat. Meas.* 44, 1109-1113.
- Wang, C., Chen, A., Chen, I., 2006. Preparation of a highly luminescent nanocomposite by chelating copolymer. *Polym. Adv. Technol.* 17, 598-603.



- Xing, Y., Xia, Z., Rao, J., 2009. Semiconductor Quantum Dots for Biosensing and In Vivo Imaging. IEEE Trans. Nanobioscience. 81, 4-12.
- Yaffe, M., Mainprize, J., Jong, R. 2008. Technical developments in mammography. Health Phys. 95(5), 599-611.
- Yanagida, T., Fujimoto, Y., Watanabe, K., 2014. Dopant concentration dependence on radiation induced positive hysteresis of Ce:GSO and Ce:GSO. Radiat. Meas. 61C, 16-20.
- Zych, E., Meijerink, A., de Mello Donega, C., 2003. Quantum efficiency of europium emission from nanocrystalline powders of  $\text{Lu}_2\text{O}_3$ : Eu. J. Phys. Condens. Matter. 15, 5145-5155.

## List of figures

**Fig. 1.** Experimental set-up for the measurement of the emitted light energy flux comprising the integrating sphere, the PMT and the vibrating reed electrometer.

**Fig. 2.** X-ray spectra measured with the portable CdTe spectrometer.

**Fig.3.** Spectra for Type I measurements. The sub-figures refer to the (a) Type A and (b) Type B UV measurements. The differences in the conditions of the UV excitation are shown in the legend. Spectra are normalised to unity and N.I. is the normalised intensity. The legend provides information regarding the employed optical barriers.

**Fig.4.** Spectra the industrial (initial) Lumidot samples (iLs) for Type I measurements. The sub-figures refer to the (a) Type A (tm) and (b) Type B (rm) UV measurements according to equation (12). All the spectra are normalised to unity, and N.I. is the normalised intensity. The N.I. of only these spectra was calculated from equation (12). The terms tm and rm refer to transmission mode and reflection mode respectively. The term iLs refers to the industrial (initial) QD sample.

**Fig.5.** Transmission spectrum of the industrial (initial) Lumidot sample for Type II measurements.

**Fig.6.** Normalised optical spectrum of the CdSe/ZnS QD nanocrystals of the industrial Lumidot samples.

**Fig.7.** (a) Electrical current time series from an excitation of the Lumidot QD samples of concentration of  $28.5 \times 10^{-5}$  mg/mL with medical x-rays for 2500 ms at 120 kV peak voltage; (b) Spearmans correlation coefficient associated with the DFA method; (c) DFA slope with time through the sliding window technique. Window length 32 ms and step 1 ms; (d) Wavelet scalogram with a log-Gabor filter of 128 scales. The

colorbar indicates the power of the amplitude of the wavelet transform.

**Fig.8.** DFA scatter plots according to technique II of section 2.2.2.1 (bottom row of figures). The corresponding time series of the electrical signals are presented in the top row of figures. The windows in red contour refer to the two discrete windows with a chaotic long-memory regime according to the technique I of section 2.2.2.1. The top left and right figures are the zoomed versions of the contoured time series.

**Fig.9.** Two example cases of averaged Fourier periodograms of the data of the (a) 120 kVp and (b) 129 kVp X-ray irradiation of the QD samples. The colours depict the different solutions: Green represents the 14.2 mg/mL, Red represents the 21.3 mg/mL and black the 28.4 mg/mL.

**Fig.10.** Absolute efficiency versus x-ray tube voltage and concentration for the Lumidot CdSe/ZnS 640 Quantum Dot samples. The legend indicates the concentrations addressed.

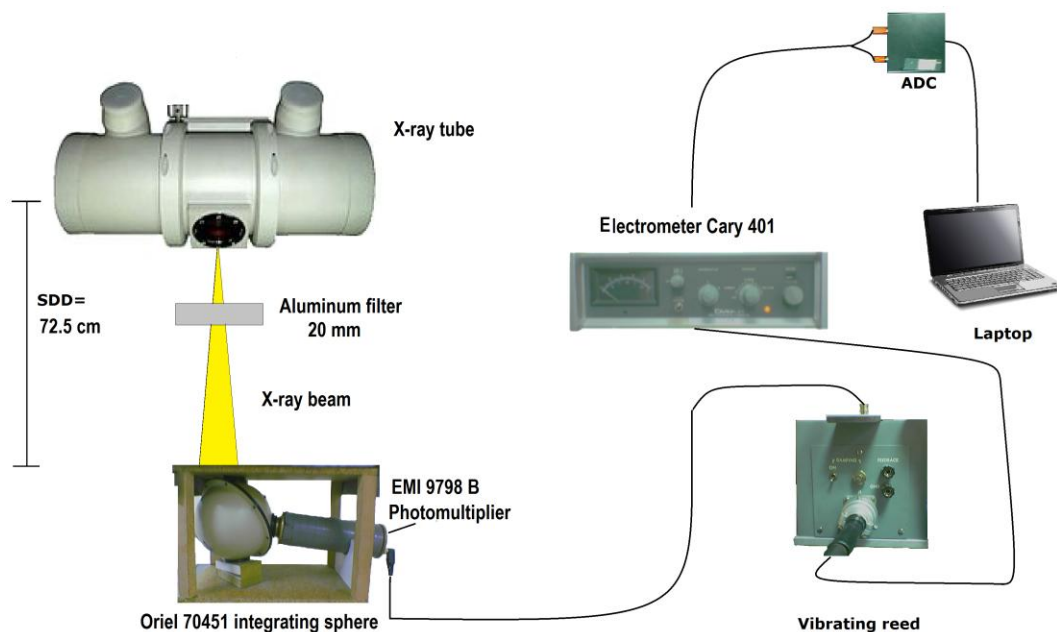


**Fig. 1**

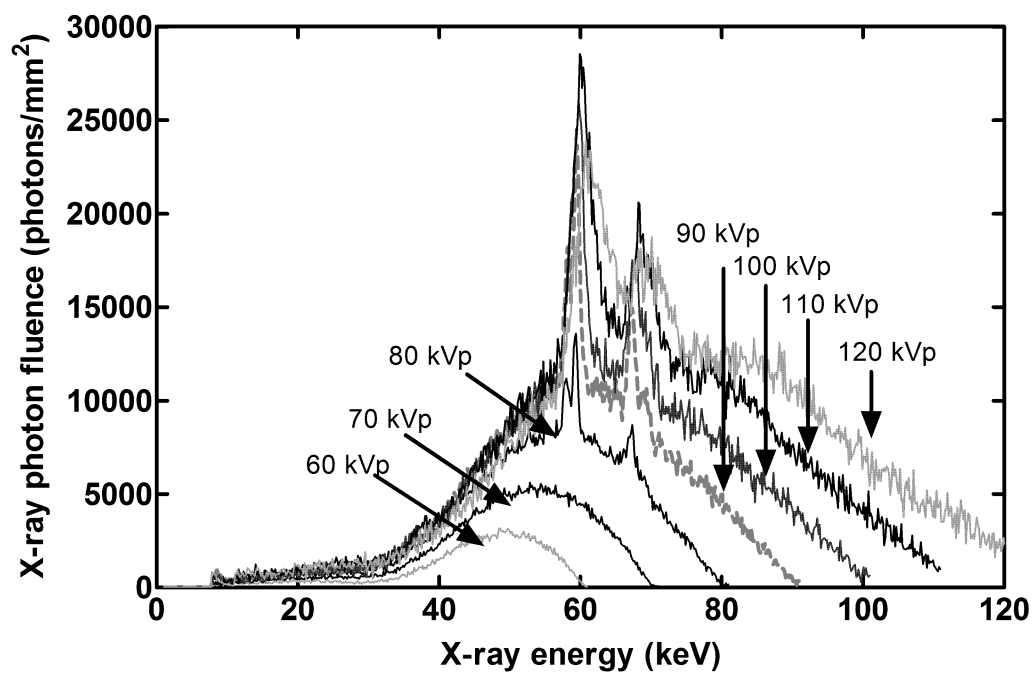
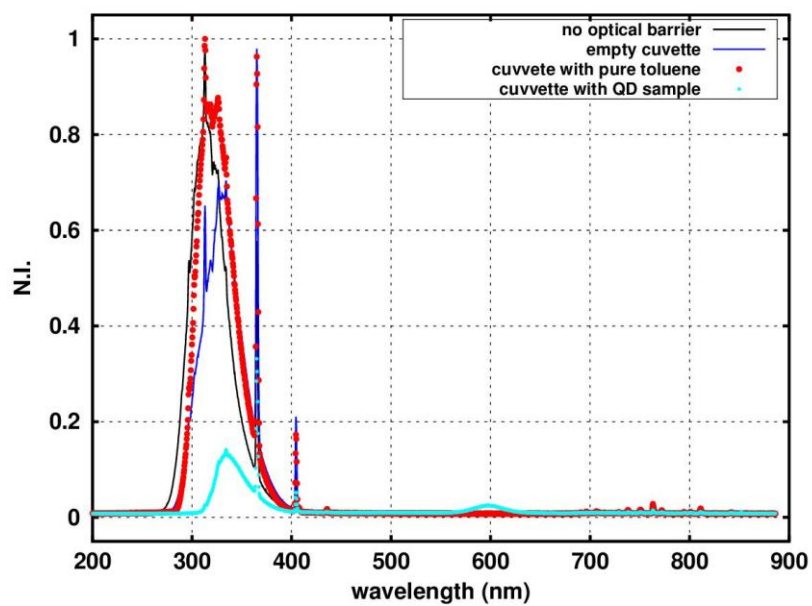


Fig. 2

(a)



(b)

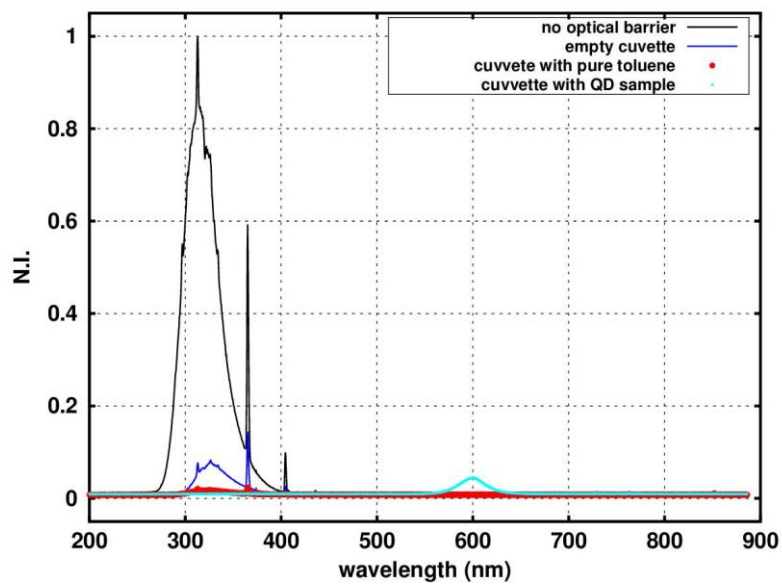
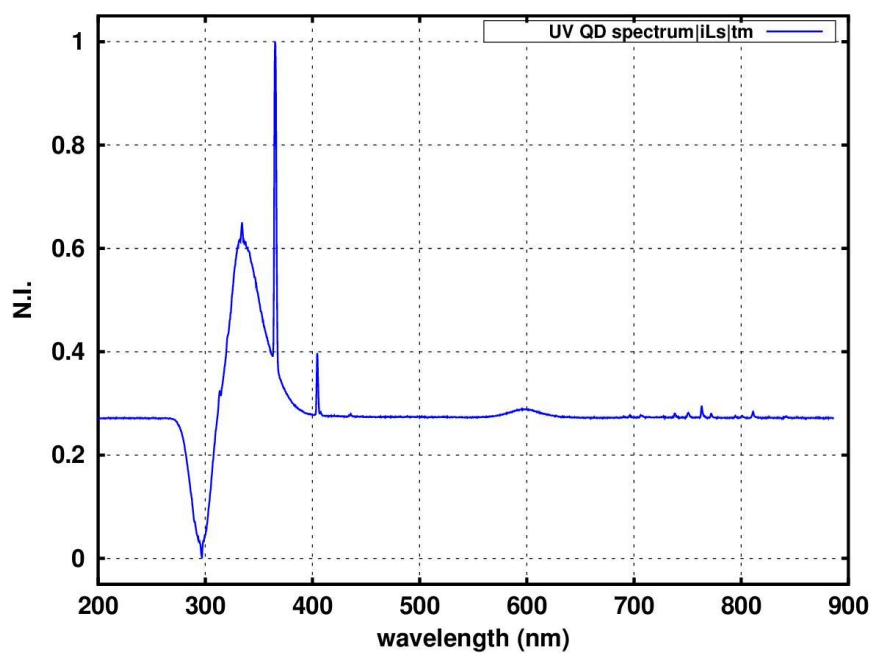


Fig. 3

(a)



(b)

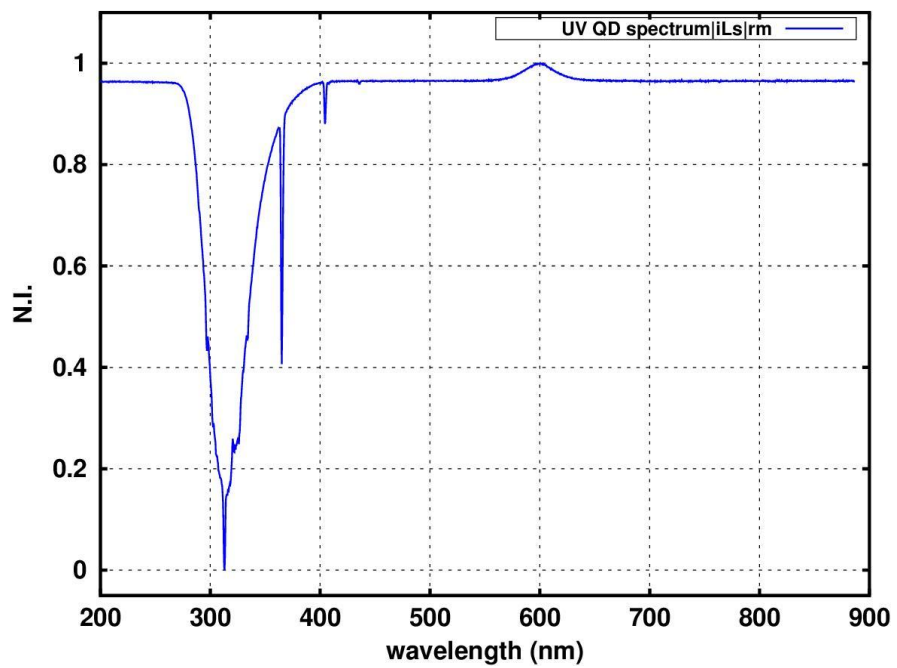


Fig. 4

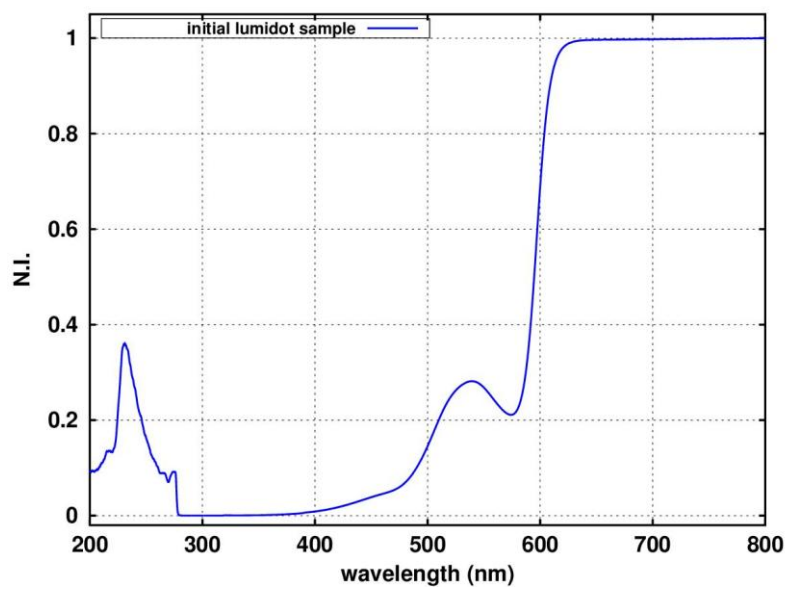


Fig. 5

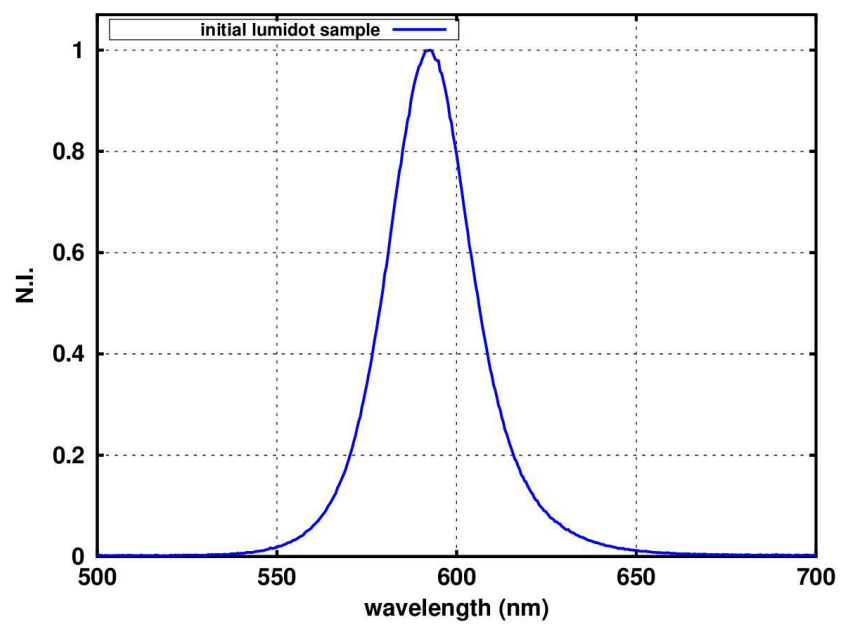
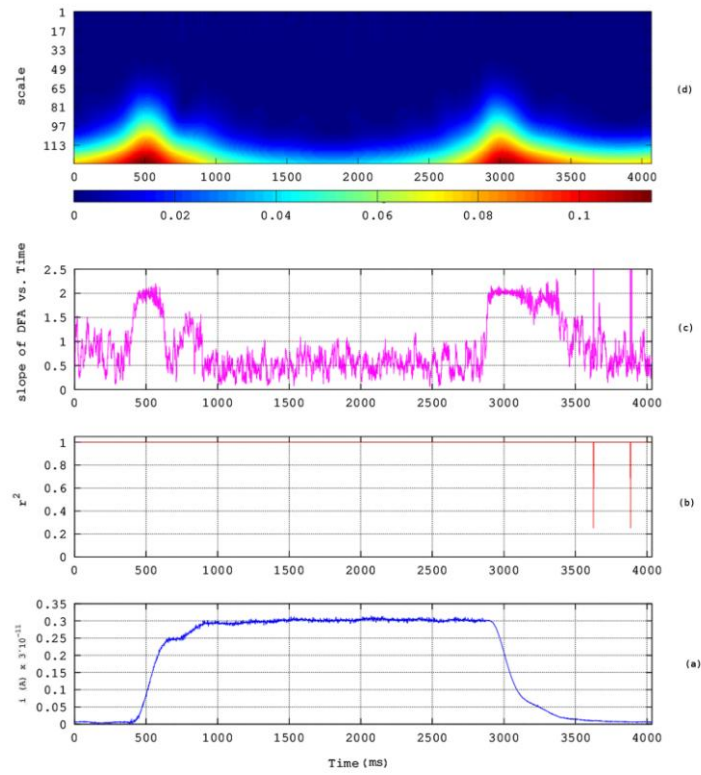


Fig. 6



**Fig. 7**



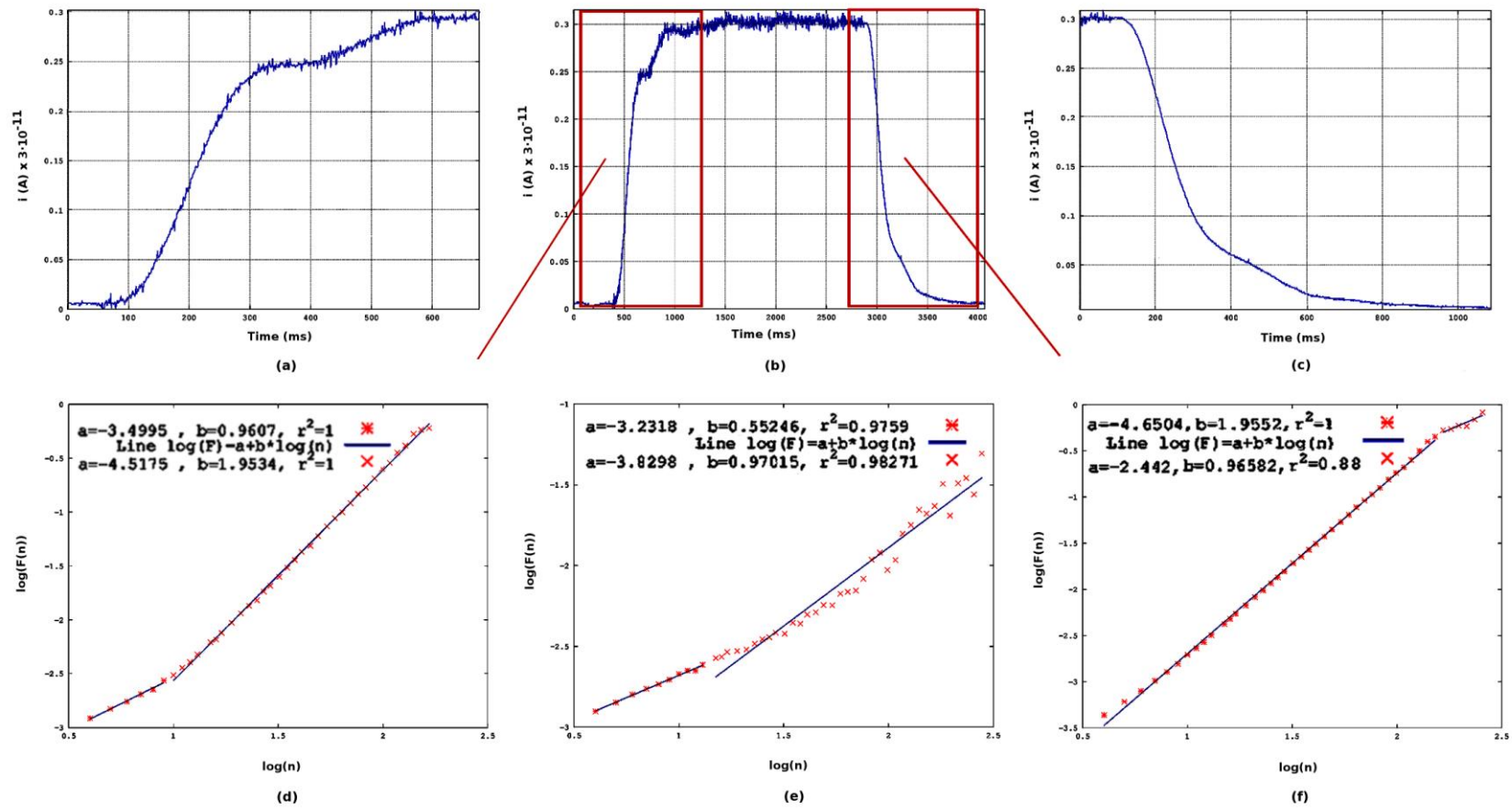
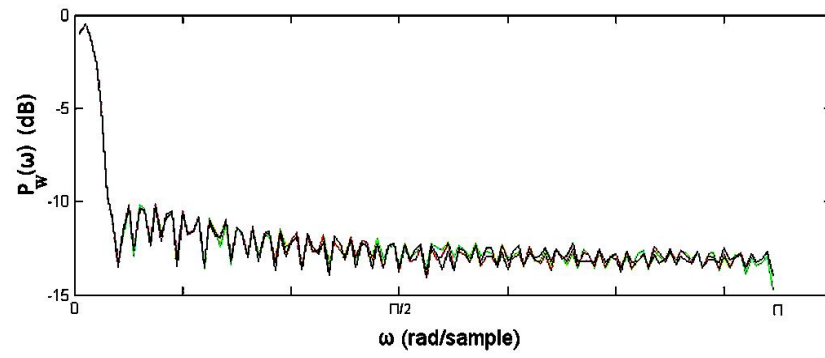


Fig. 8

(a)



(b)

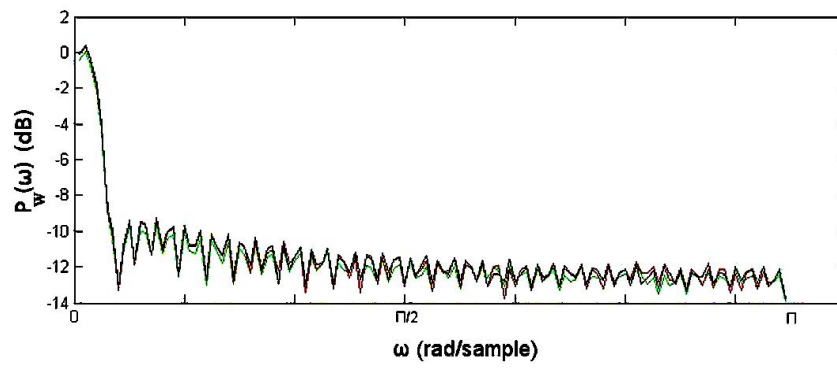
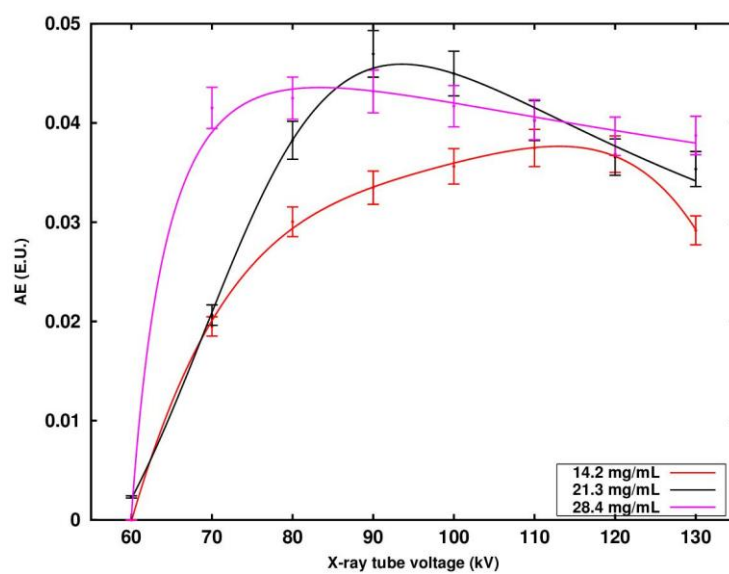


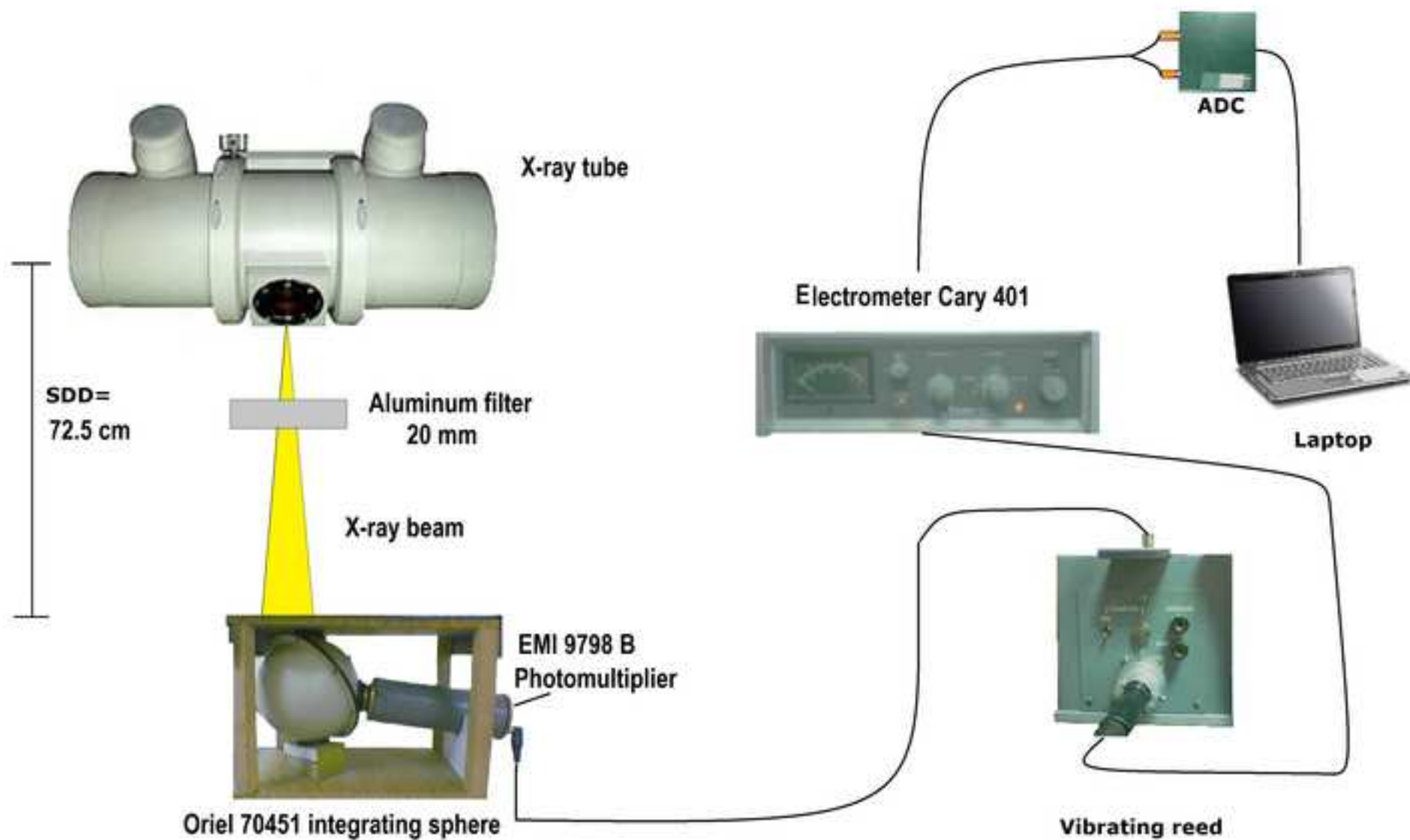
Fig. 9



**Fig.10**

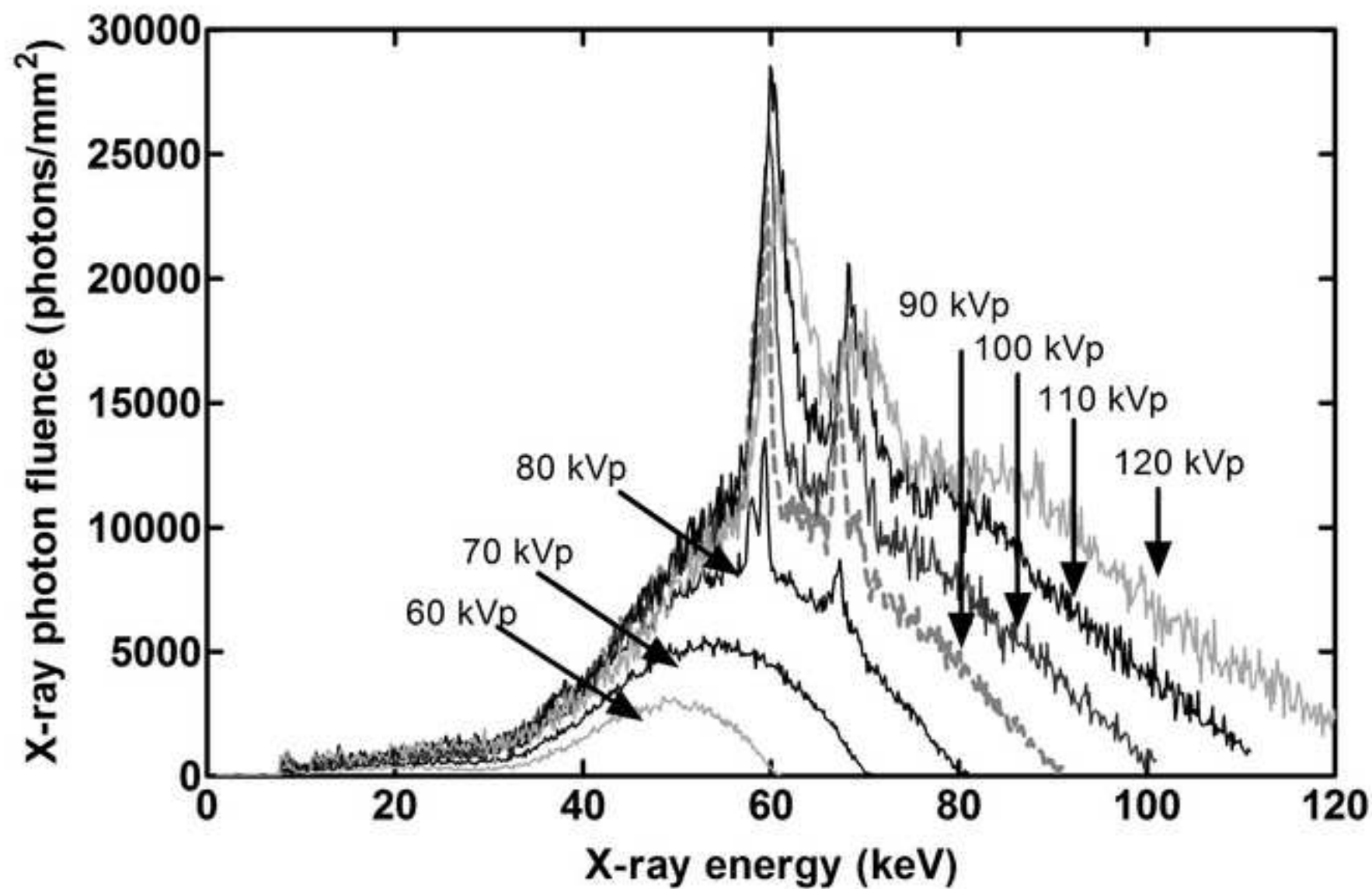
Figure

[Click here to download high resolution image](#)



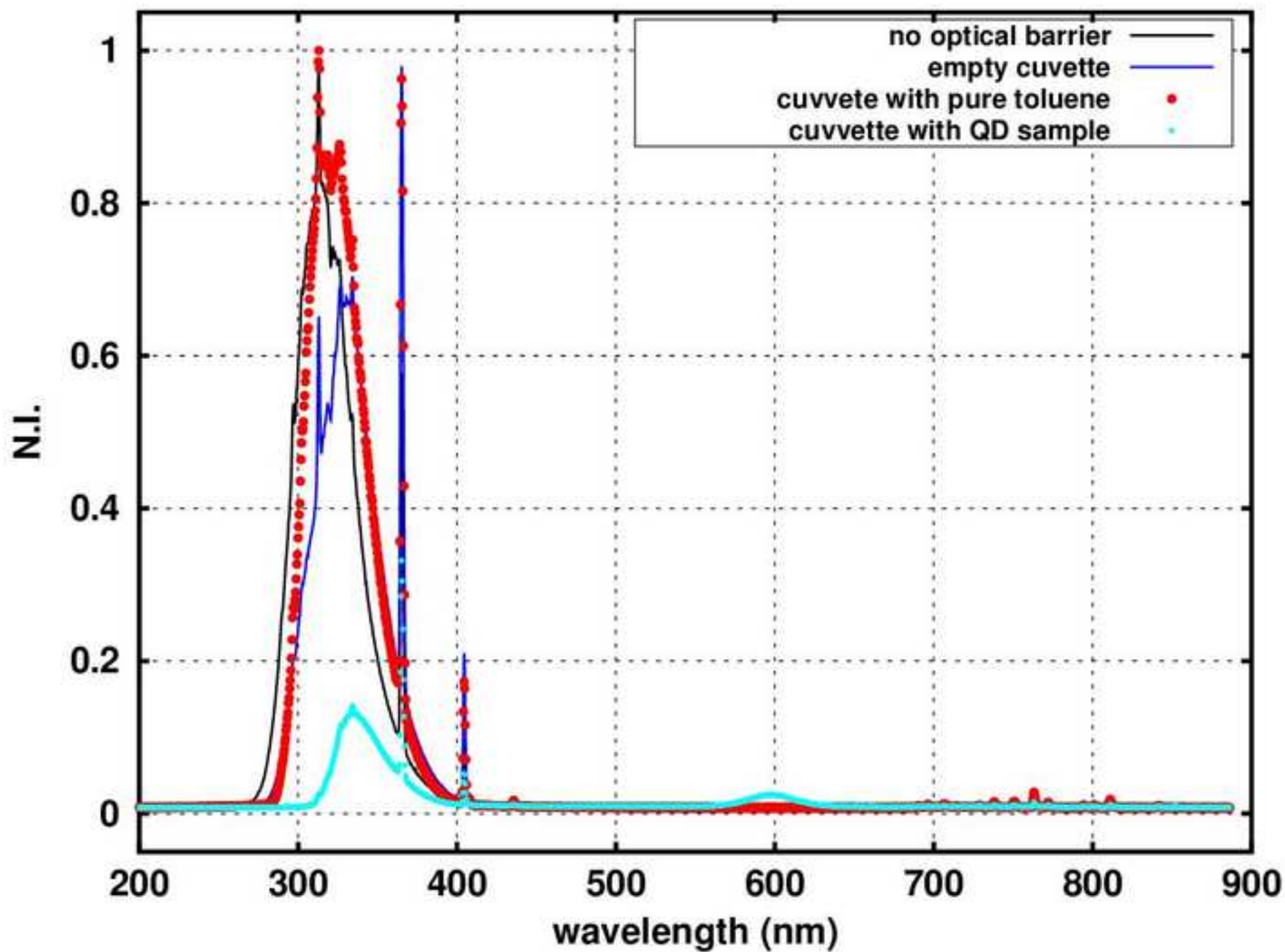
Figure

[Click here to download high resolution image](#)



Figure

[Click here to download high resolution image](#)



Figure

[Click here to download high resolution image](#)

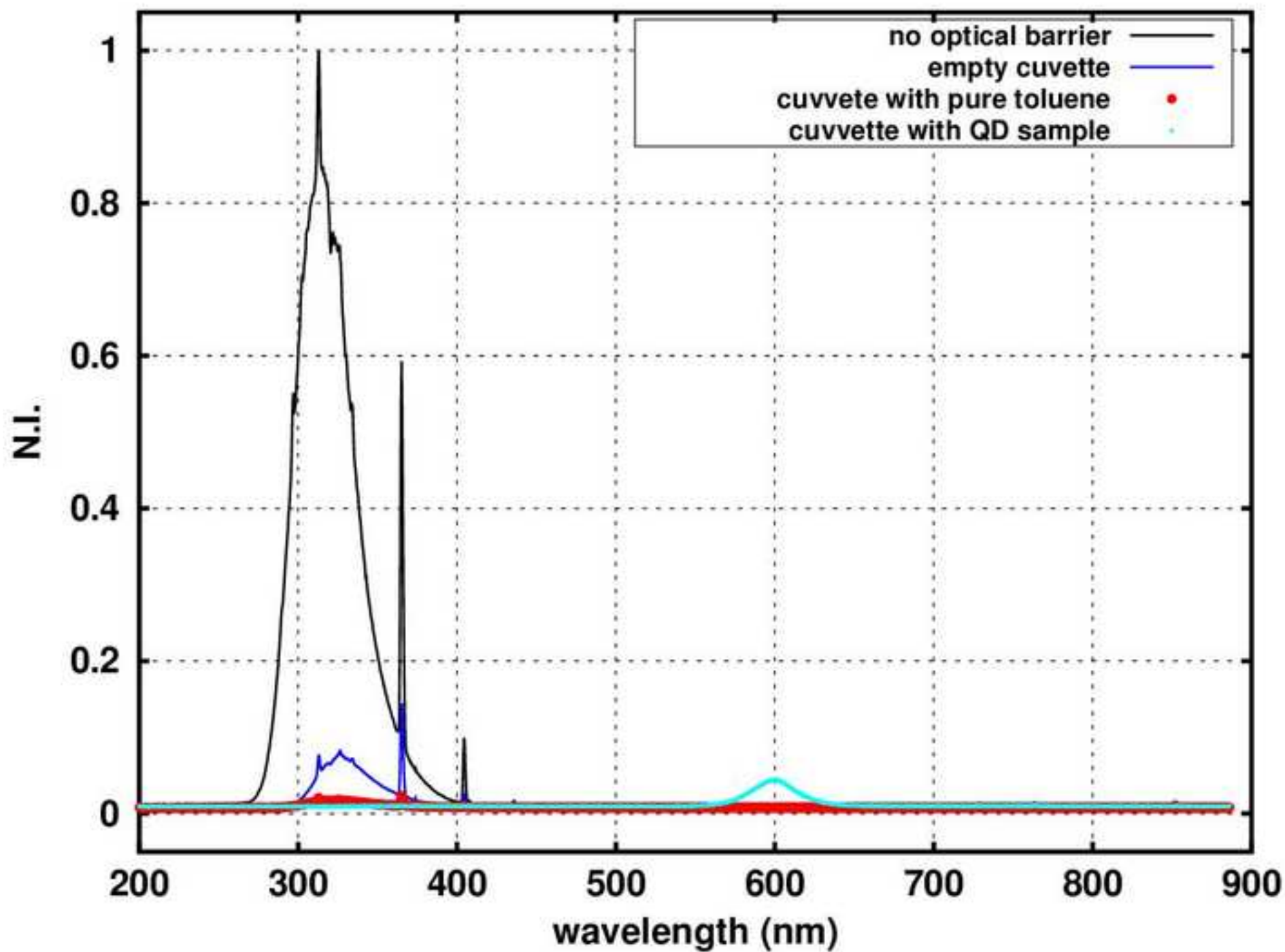




Figure  
[Click here to download high resolution image](#)

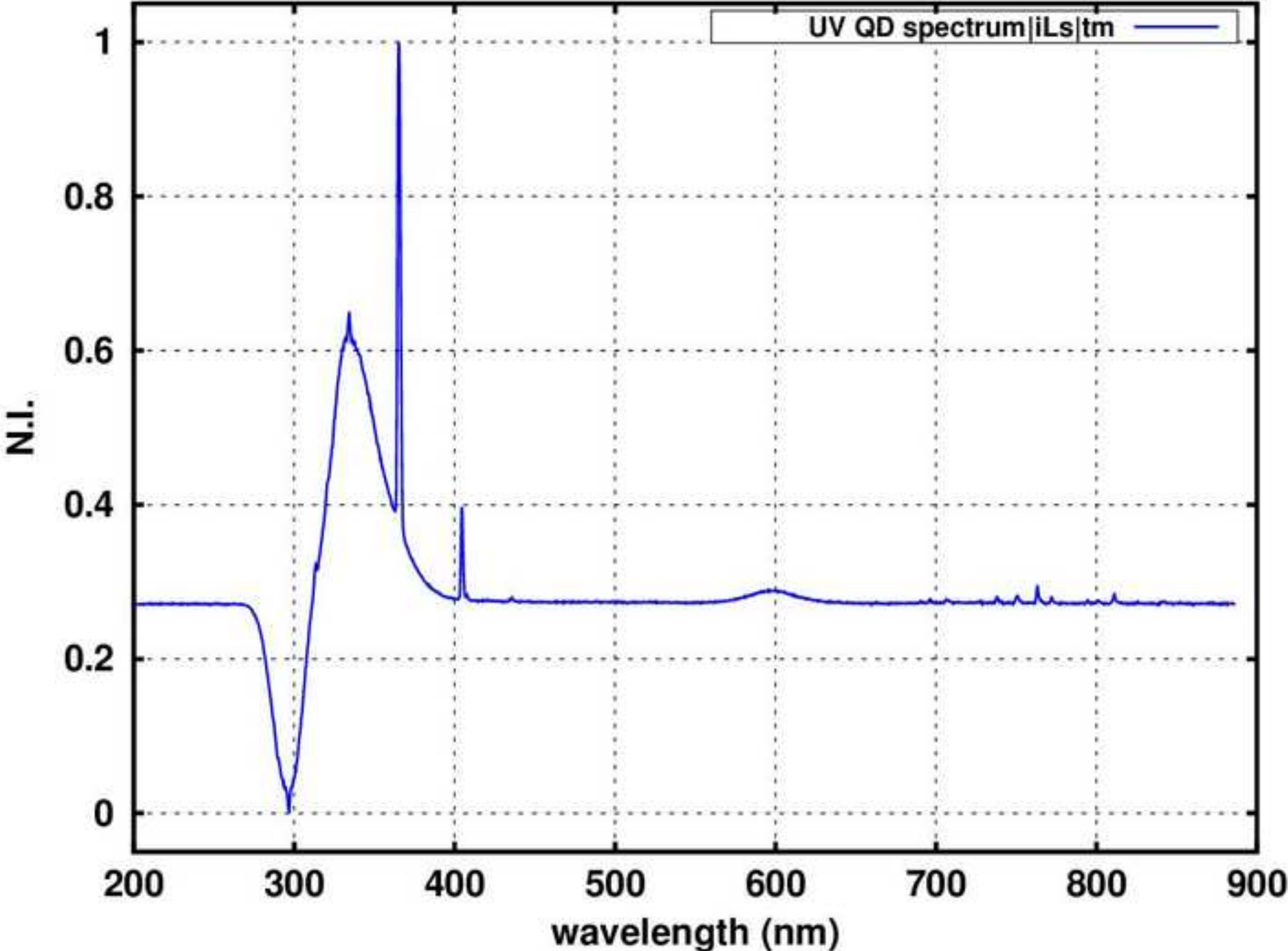
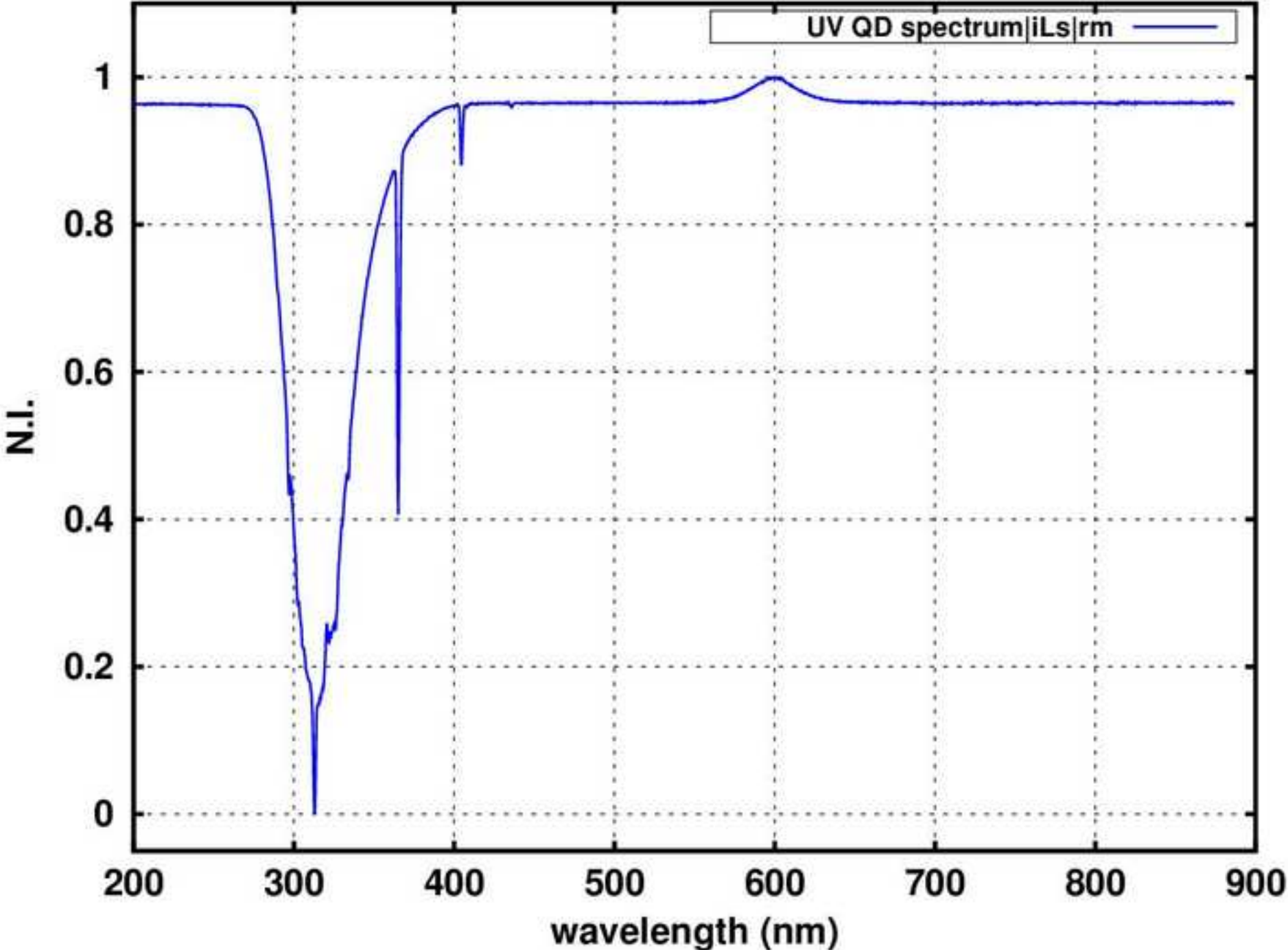


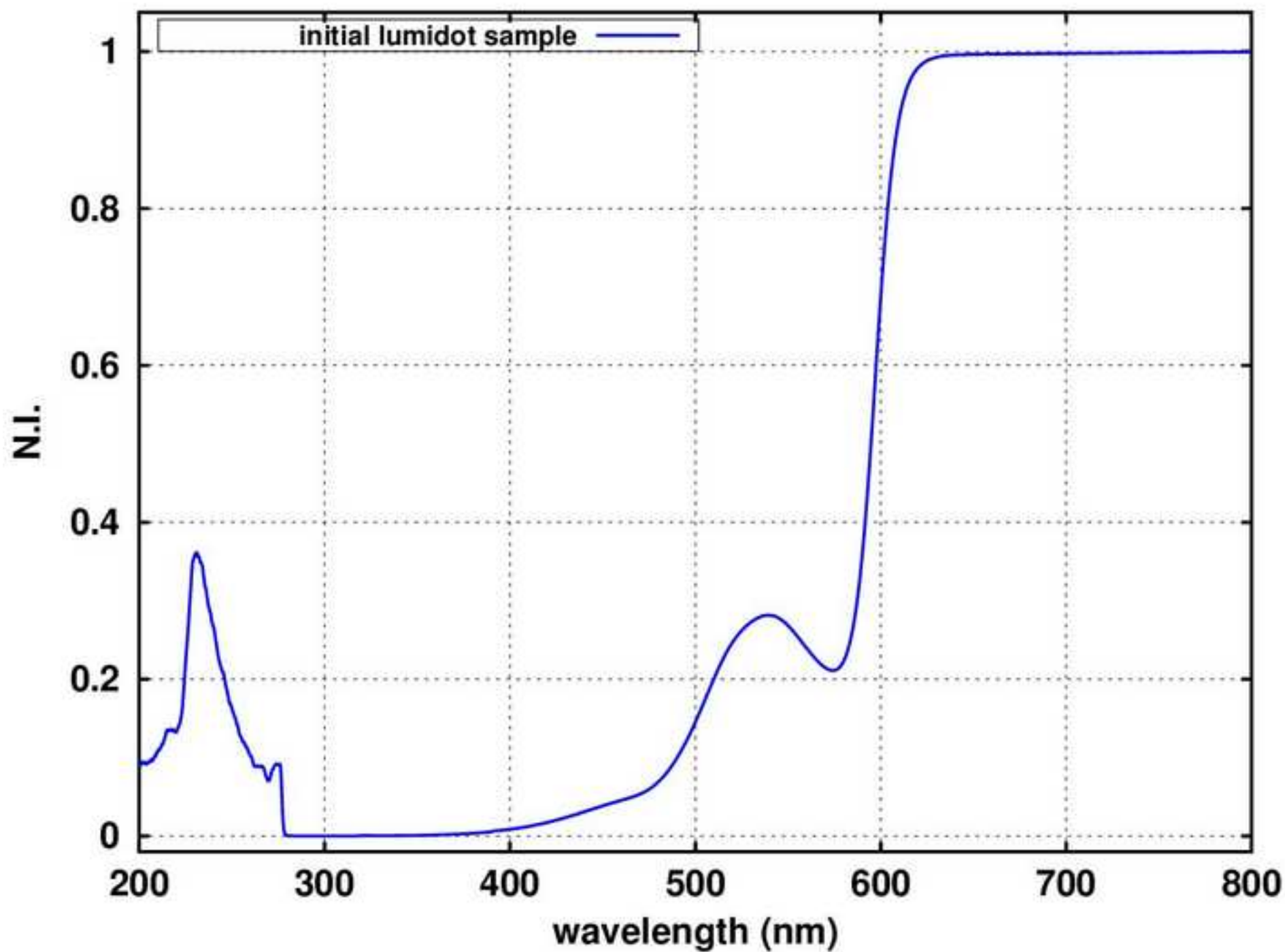


Figure  
[Click here to download high resolution image](#)



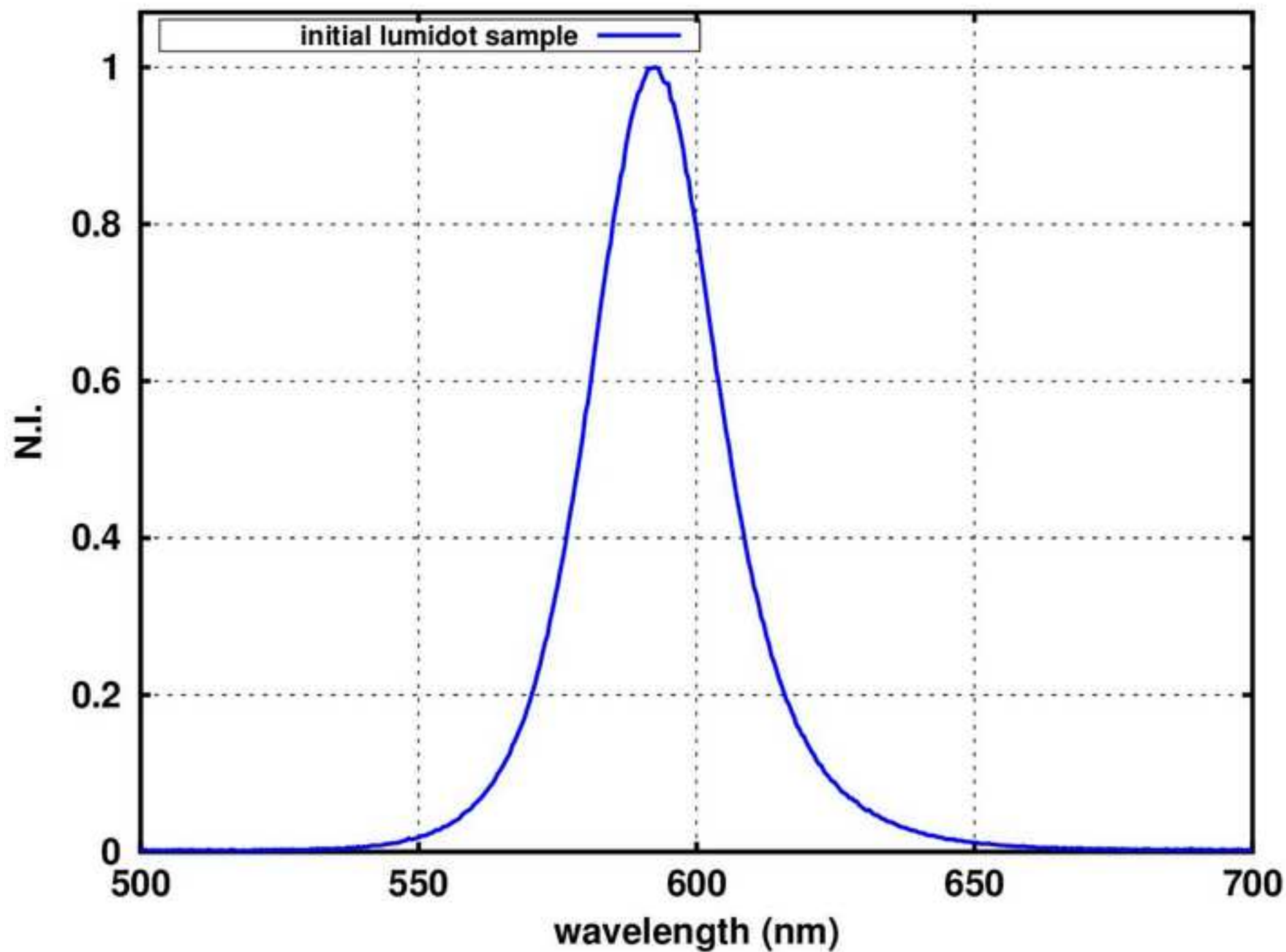
Figure

[Click here to download high resolution image](#)



Figure

[Click here to download high resolution image](#)



Figure

[Click here to download high resolution image](#)

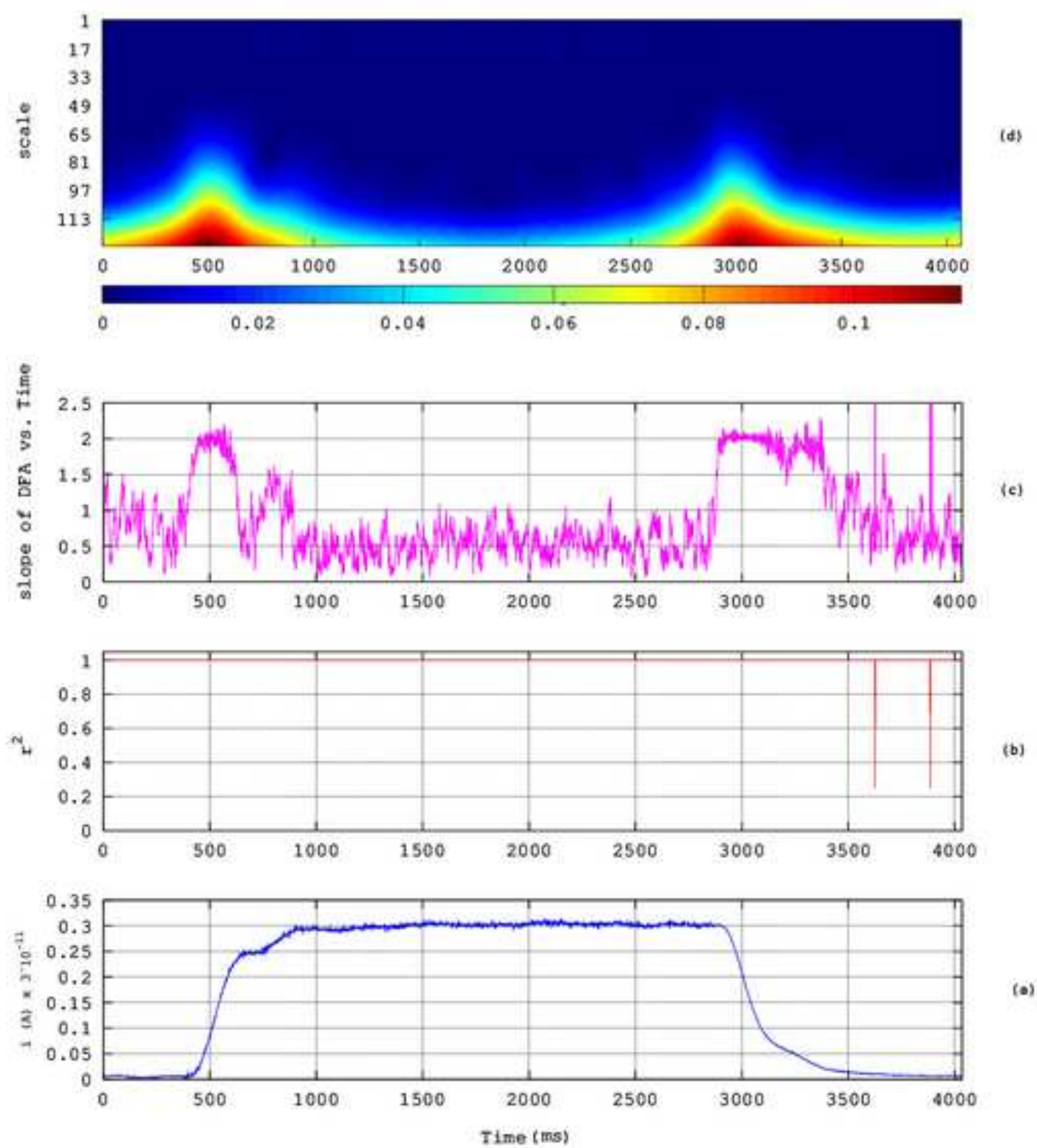
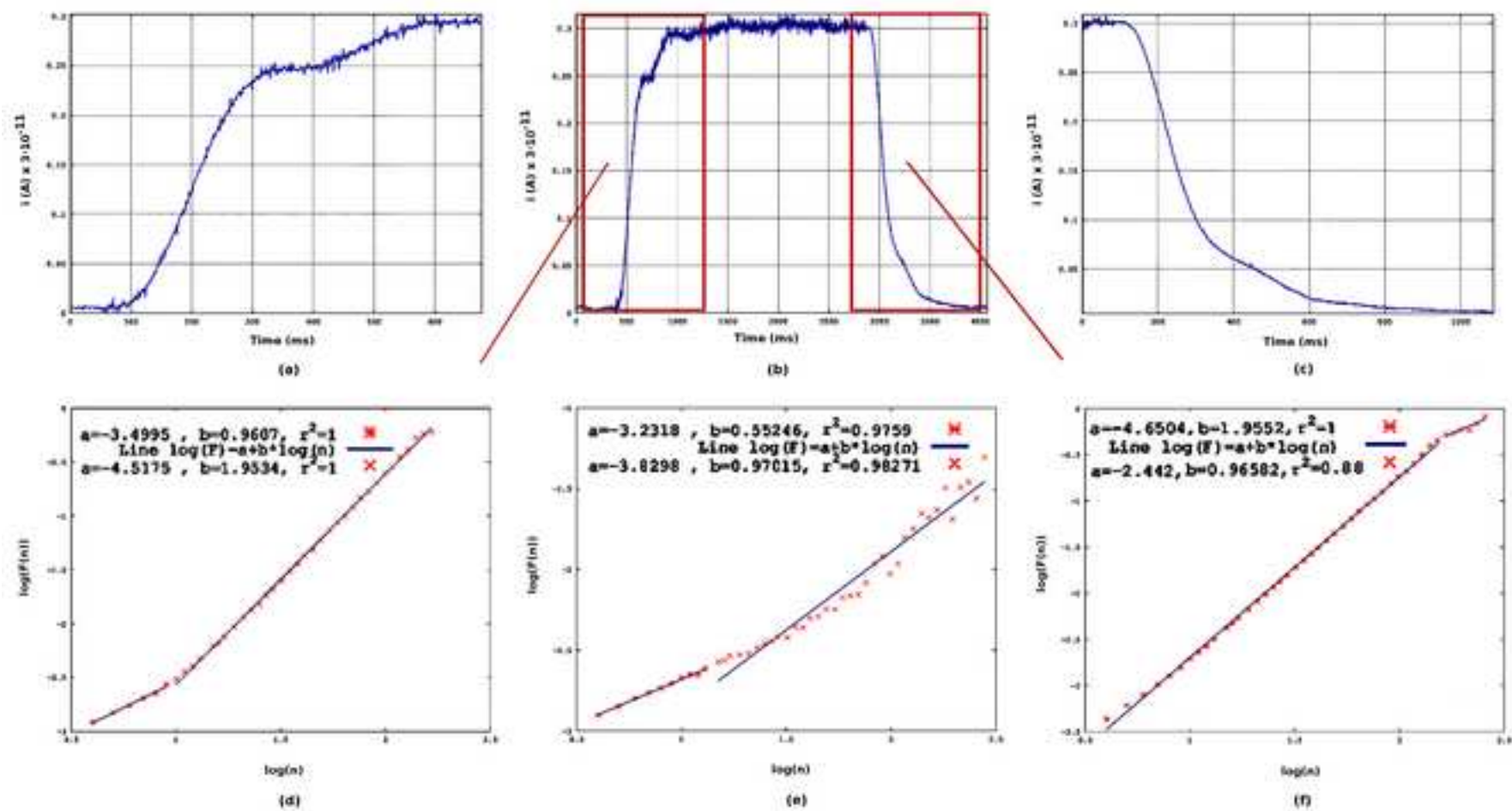
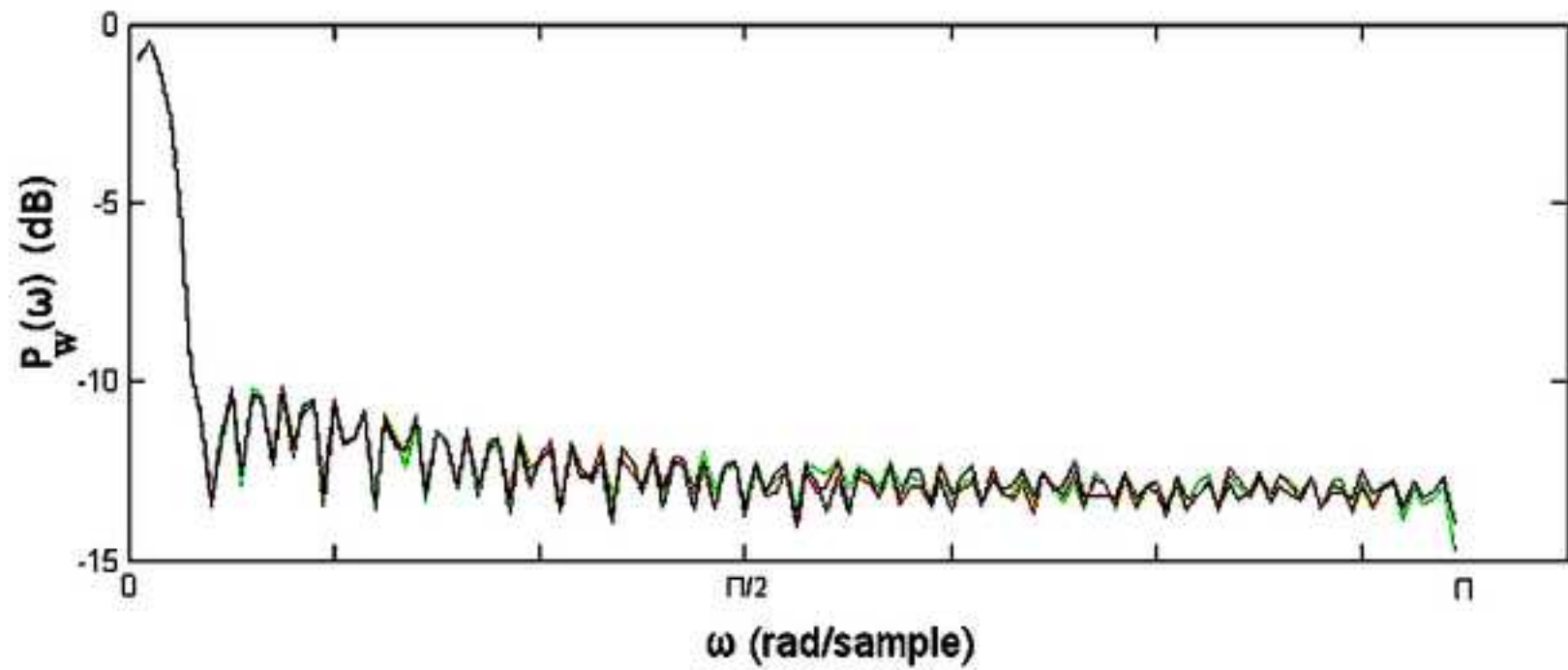


Figure  
[Click here to download high resolution image](#)



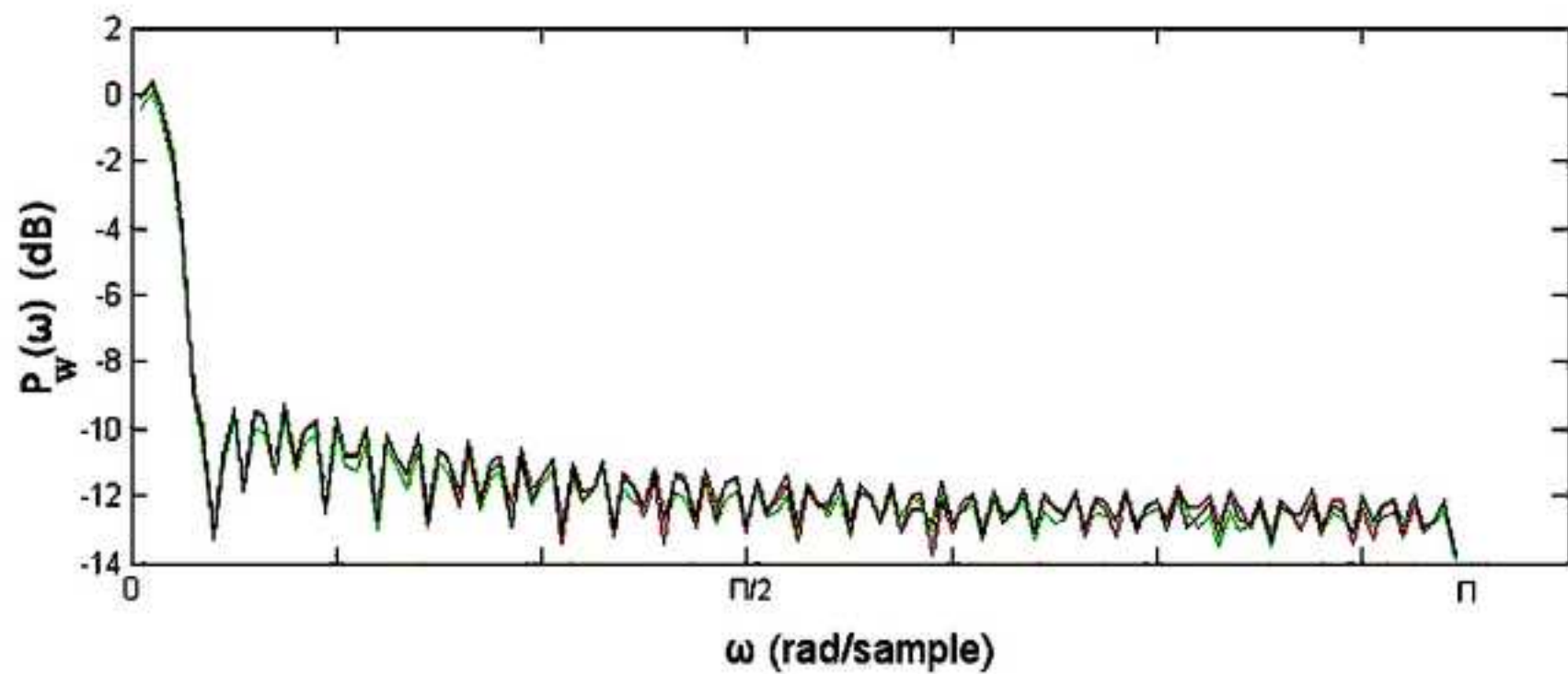
Figure

[Click here to download high resolution image](#)



Figure

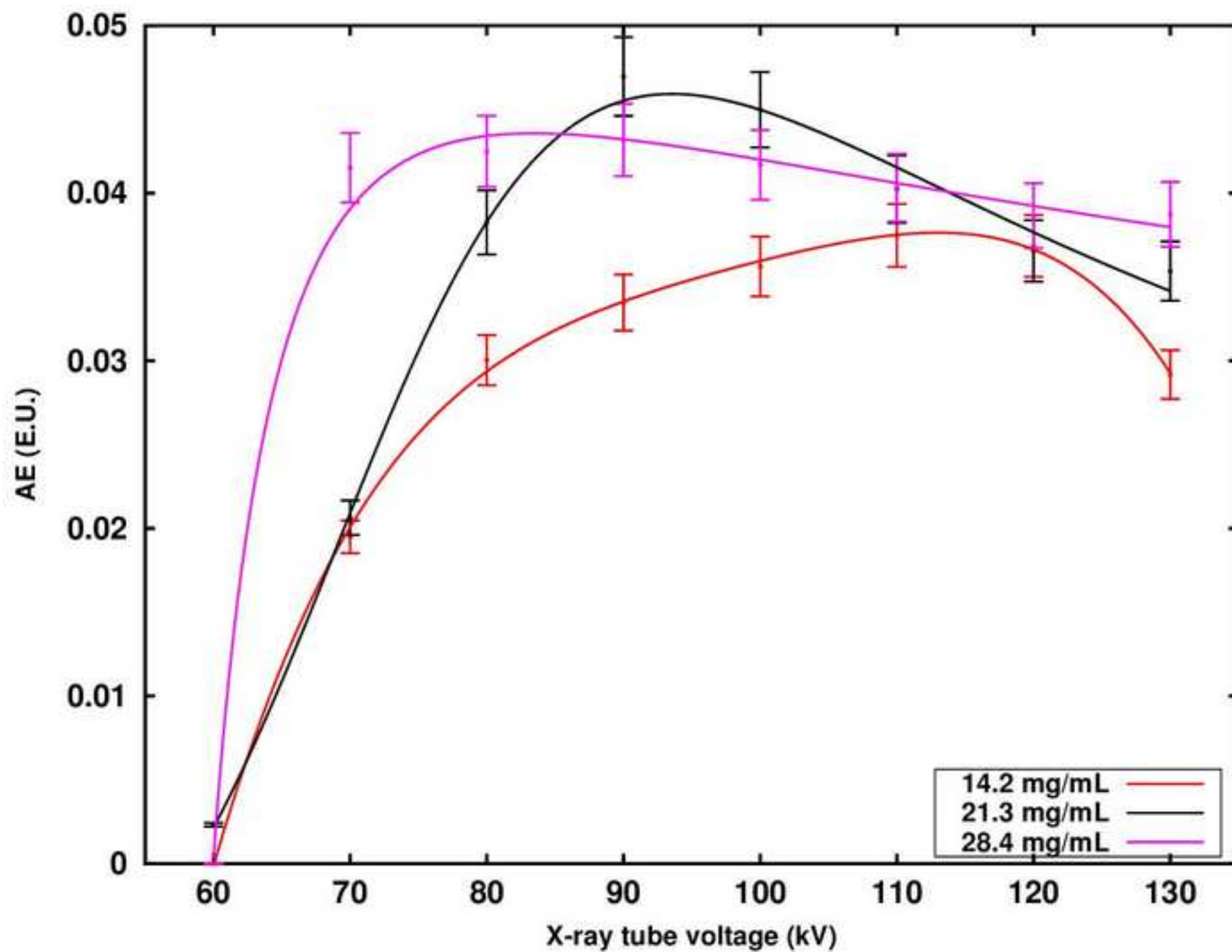
[Click here to download high resolution image](#)





Figure

[Click here to download high resolution image](#)





- Luminescence properties of CdSe/ZnS QDs under UV and X-ray irradiation
- Detrended fluctuation analysis used to identify long-memory trends in the signal
- QDs of high concentrations exhibited high absolute efficiency up to 80 kVp
- CdSe/ZnS showed potential for detection of X-rays in the medical imaging energies

2016-06-14

# Radioluminescence properties of the CdSe/ZnS Quantum Dot nanocrystals with analysis of long-memory trends

Nikolopoulos, D.

Elsevier

---

D. Nikolopoulos, I. Valais, C. Michail, A. Bakas, C. Fountzoula, D. Cantzos, D. Bhattacharyya, I. Sianoudis, G. Fountos, P. Yannakopoulos, G. Panayiotakis, I. Kandarakis, Radioluminescence properties of the CdSe/ZnS Quantum Dot nanocrystals with analysis of long-memory trends, Radiation Measurements, Volume 92, September 2016, pp19-31

<http://dx.doi.org/10.1016/j.radmeas.2016.06.004>

*Downloaded from Cranfield Library Services E-Repository*